2018

HIGH RESOLUTION DATA ACQUISITION SYSTEM FOR BRAIN IMAGING

Seyed Hadi Nasrollaholhosseini
University of Rhode Island, hadi.n.hosseini@gmail.com

HIGH RESOLUTION DATA ACQUISITION SYSTEM FOR BRAIN IMAGING

BY

SEYED HADI NASROLLAHOLHOSSEINI

A DISSERTATION SUBMITTED IN PARTIAL FULFILLMENT OF THE

REQUIREMENTS FOR THE DEGREE OF

DOCTOR OF PHILOSOPHY

IN

ELECTRICAL ENGINEERING

UNIVERSITY OF RHODE ISLAND

2018

DOCTOR OF PHILOSOPHY DISSERTATION

OF

SEYED HADI NASROLLAHOLHOSSEINI

APPROVED:

Dissertation Committee:

Major Professor Godi Fischer

Walter G. Besio

Alan J. Davis

Otto J. Gregory

Nasser H. Zawia

DEAN OF THE GRADUATE SCHOOL

UNIVERSITY OF RHODE ISLAND

2018

ABSTRACT

The U.S. has 12.3% disabled people based on the American Community Survey (ACS) in 2012. According to this survey, more than half of the disabled population suffers from ambulatory disabilities. Therefore, a system which enables people with disabilities to control their environments is crucially important. Moreover, ubiquitous physiological monitoring will be a key driving force in the upcoming medical revolution. Cardiac and brain signals in the form of electrocardiograms (ECGs) and electroencephalograms (EEGs) are two critical health indicators that directly benefit from long-term monitoring.

Brain-computer interfaces (BCIs) are systems that detect changes in brain signals related to human intentions, typically translating intention into a control signal to communicate between the brain and the external world such as a computer. The tripolar concentric ring electrode (TCRE) has shown to be sensitive enough to visualize the electrical impulses that correspond to a person's specific thought pattern. Therefore, this electrode has the potential to enable people who are paralyzed to use their thoughts to control their phone, television or other things in their environment.

The TCRE has been built and was successfully tested. However, at this step of its development, long coaxial cables are required to connect the electrodes to the preamplifier. The preamplifier is a big box with 24 channels (for 24 electrodes), although not all channels are always used. Despite technologically advancements and electronic miniaturization, the use of current EEG monitoring is limited by inconvenience and discomfort. Thus, having an active TCRE EEG electrode that can record the signal, digitize it and send the data to the host computer for further processing is helpful. Such a system not only preserves the advantages of the TCRE electrode, but also takes advantage of today's advancement in microelectronics. This renders the electrode more comfortable and convenient to be used in real life situations. Therefore, the EEG acquisition

board has to be miniaturized so that it fits on the electrode. The small board can also be duplicate many times to meet the needs of a specific EEG recording application.

Our approach to build an active TCRE acquisition system (digital TCRE) involves two steps:

Step 1: create a mathematical model of the electrode, electrolyte, and body may contribute to a better understanding of how biomedical signals are obtained by electrodes. Good design starts with clearly understanding and defining interface requirements and developing accurate equivalent circuit models of all components involved.

In order to understand the behavior of the interface, electrochemical impedance spectroscopy (EIS) has been used to measure the impedance on both a TCRE and standard cup electrode. To perform the experiments, Ten20 is used as an electrode paste. The preliminary results have been published in the proceedings of the Engineering in Medicine and Biology Society (EMBC) in 2016. The title of the paper is "Electrode-Electrolyte Interface Model of Tripolar Concentric Ring Electrode and Electrode Paste". More experiments were carried out with different pastes to measure the characteristics of the electrodes with various electrolyte materials. These findings have been published in the proceedings of the Engineering in Medicine and Biology Society (EMBC) in 2017. The title of the paper is "Impedance Spectroscopy of Tripolar Concentric Ring Electrode with Ten20 and TD246 Pastes". In this paper the impedance characteristics of electrode using Ten20 and TD246 as electrolyte material is shown. Finally, more measurements with two electrode setup and three electrode setup were done using EIS. The findings have been submitted to the Transaction on Biomedical Engineering (TBME). The title of the manuscript is "Electrode-Electrolyte Interface Modeling and Impedance Characterization of Tripolar Concentric Ring Electrode". This paper introduces a model for a tripolar concentric ring electrode (TCRE) derived from impedance measurements using the Ten20 electrode impedance matching paste. It is shown that the model serves

well to predict the performance of the electrode-electrolyte interface for TCREs as well as standard cup electrodes. The paper also presents a comparison between the TCRE and the standard cup electrode regarding their impedance characterization and demonstrates the benefit of using TCREs in biomedical applications. We have also conducted auditory evoked potential experiments using both TCRE and standard cup electrodes.

Step 2: design and fabricate a system level circuit for monitoring the TCRE outputs have started with commercial off-the-shelf components (COTS). Subsequently, we will design and fabricate an application specific circuit (ASIC) that digitizes the EEG signatures at the front-end and sends the acquired data to a host PC.

To accomplish this, a delta sigma based data converter has been designed and fabricated. Preamplifier and the data converter have been mounted on two pcb boards with 15mm diameter. The results are under preparation for submission to a peer reviewed journal. The title of the manuscript is “Digital Tripolar Concentric Ring Electrode for Biopotential Signal Recordings”.

ACKNOWLEDGMENTS

Firstly, I would like to express my deepest gratitude to my supervisor, Prof. Godi Fischer, for his advise, guidance, and help in developing my skills specifically in designing integrated circuits throughout the years. I learned a lot from him. I would also like to express my sincere thanks to my co-advisor, Prof. Walter G. Besio, for his encouragements and support throughout my research. It has been a great opportunity for me to gain my knowledge in biomedical systems under his direction.

I would like to thank my committee member Prof. Otto Gregory and Prof. Alan J. Davis for reviewing my dissertation and sharing their knowledge and providing help.

I would also like to thank Prof. Jien-Chung Lo, Dr. Soheil Hashemi, Will Simoneau for their support and help with FPGA design. I would like to thank Prof. Richard Brown in chemical engineering for letting me to use the EIS tools. It help me to understand the electrode characterization a lot. I would also like to thank my fellow students at the University of Rhode Island specially my previous and current friends at the Neurorehabilitation lab and Wearable Biosensing lab. Thanks also goes to all of my friends for their support and help to make this happen.

Most importantly, I would like to thank my parents whose love and sacrifices are with me in whatever I pursue and I hope I have made their support worthwhile. I would also like to thank my brother, and my two sisters, Sanaz's family whose support has been very significant. Last but not least, I would like to express my gratitude to my wife, Sanaz, for all of her patience, support and love.

PREFACE

This dissertation is prepared in Manuscript Format according to the guidelines presented by the University of Rhode Island Graduate School. This dissertation consists of four manuscripts.

Masuscript 1:

S. H. Nasrollaholhosseini, P. Steele and W. G. Besio, *"Electrode-Electrolyte Interface Model of Tripolar Concentric Ring Electrode and Electrode Paste"*.

This manuscript is published in the proceedings of the Engineering in Medicine and Biology Society (EMBC), 2016 IEEE 38th Annual International Conference of the, pp. 2071-2074. IEEE, 2016.

Masuscript 2:

S. H. Nasrollaholhosseini, D. S. Herrera and W. G. Besio, *"Impedance Spectroscopy of Tripolar Concentric Ring Electrodes with Ten20 and TD246 Pastes"*.

This manuscript is published in the proceedings of the Engineering in Medicine and Biology Society (EMBC), 2017 IEEE 39th Annual International Conference of the, pp. 2426-2429. IEEE, 2017.

Masuscript 3:

S. H. Nasrollaholhosseini, J. Mercier, G. Fischer and W. G. Besio *"Electrode-Electrolyte Interface Modeling and Impedance Characterizing of Tripolar Concentric Ring Electrode"*.

This manuscript is under peer review in "Transaction on Biomedical Engineering (TBME)", IEEE.

Masuscript 4:

S. H. Nasrollaholhosseini, W. G. Besio and G. Fischer *"Digital Tripolar Concentric Ring Electrode for Biopotential Signal Recordings"*.

This manuscript is in preparation for publication and will be submitted to "Trans-

action on Biomedical Circuit and System (TBioCAS)", IEEE.

TABLE OF CONTENTS

Page

LIST OF FIGURES

LIST OF TABLES

MANUSCRIPT 1

Electrode-Electrolyte Interface Model of Tripolar Concentric Ring Electrode and Electrode Paste

Seyed Hadi Nasrollaholhosseini[1], Preston Steele[1], Walter G. Besio[1]

Published in the proceedings of the Engineering in Medicine and Biology Society (EMBC), 2016.

[1] Electrical, Computer, and Biomedical Engineering Department, University of Rhode Island, Kingston, RI 02881 USA.

abstract

Electrodes are used to transform ionic currents to electrical currents in biological systems. Modeling the electrode-electrolyte interface could help to optimize the performance of the electrode interface to achieve higher signal to noise ratios. There are previous reports of accurate models for single-element biomedical electrodes. In this paper we develop a model for the electrode-electrolyte interface for tripolar concentric ring electrodes (TCRE) that are used to record brain signals.

1.1 INTRODUCTION

Physiological systems such as the cardiovascular system, nervous system, and muscular system all generate ionic current flows in the body. Each physiological process is associated with specific signals that reflect the underlying nature and activities of each source. One such physiological signal of interest is the electroencephalography (EEG) which is the recording of brain electrical activity.

Biomedical signals can be obtained with electrodes that sense the variations in electrical potential generated by physiological processes. Electrodes convert the ionic currents flowing in the body generated by underlying cells intoelectrical currents [1]. Therefore, electrodes transduce ionic currents, in our case from the human body into electrical currents.

A mathematical model of the electrode, electrolyte, and body may help us to have a better understanding of how biomedical signals are obtained by electrodes.Since electrodes act as transducers, we need to understand the mechanisms that generate the transduction process between the electrode and the human body. Moreover, physiological processes in the human body generate ionic current flows in the volume conductor, the body. Hence, at the contact site of an electrode to the body an electrode-electrolyte interface forms. Figure 1.1 shows the contact of an electrode to an electrolyte. At the interface of electrode-electrolyte, chemical reactions take place that can be shown by

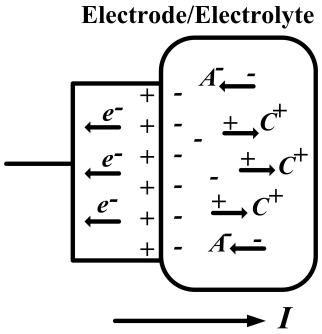

Figure 1.1. Electrode-Electrolyte Interface

the following equations [2]:

$$C \Leftrightarrow C^{n+} + ne^{-} \tag{1.1}$$

$$A^{m-} \Leftrightarrow A + me^{-} \tag{1.2}$$

There are some considerations regarding the above equations and the electrode-electrolyte interface. First of all, Equation (1) shows the oxidation reaction from left to right, and the reduction reaction from right to left, and both reduction and oxidation can occur at the electrode-electrolyte interface. Secondly, Equation (1) shows that for current-ion exchange at the interface, we should place a metal (C) into an aqueous solution containing ions of the metal (C+). Thus, there is oxidation and cations are dispersed into the electrolyte and electrons are left in the electrode. Equation (2) shows that the anions (A) can also be oxidized to a neutral atom and release one or more electrons by moving to the interface.

Obtaining an accurate model for the electrode-electrolyte interface is complicated and has been studied for many years. The concept of the electric double layer was first proposed by Helmholtz in 1879 [3]. He found that at the electrode-electrolyte interface, since the electrolyte is saturated with charged electrons, the ions with the same charges will be pushed back while the opposite charges will be attracted. Therefore, at the electrode-electrolyte interface there will be two compact layers of opposite charges

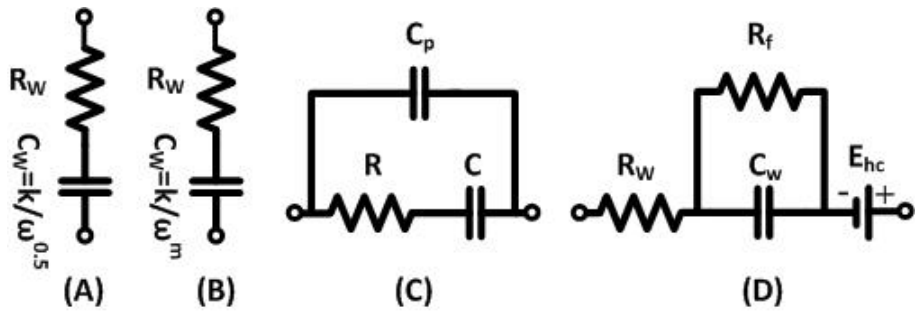

Figure 1.2. Electrical circuit model evolution of the electrode-electrolyte interface. (a) Warburg, (b) Fricke (c) Randles, and (d) Geddes and Baker models

called the electric double layer (EDL).

In 1899 Warburg proposed the first electrode-electrolyte model. He proposed a series combination of a capacitor and resistor in which the magnitude of the reactance and resistance is dependent on the electrode type, area (including surface conduction), the electrolyte, the frequency, and the current density [4]. In the Warburg model Rw and Cw, were proposed for infinitely low density current, which decreases by the square root of frequency as the frequency increase $\frac{1}{\sqrt{f}}$. This model is depicted in Fig. 1.2a.

In 1932 Fricke proposed a similar model for the electrode-electrolyte interface with the Warburg combination of series resistor and capacitor, adding that $C_W = \frac{K}{\omega^m}$. So in the proposed Fricke model which is shown in Fig. 1.2b the Warburg reactance and resistance are as follows:

$$X_\omega = \frac{1}{k\omega^{1-m}} \tag{1.3}$$

$$X_\omega = \frac{X_\omega}{tan\frac{m\pi}{2}} \tag{1.4}$$

where k and m depend on the metal species. In 1947 Randles suggested another popular model for electrode-electrolyte interface [4]. In the Randles model, depicted in Fig. 1.2c, a double-layer capacitance (Cd) was added in parallel with a series combination of resistance (R) and capacitance (C). However, the above mentioned models do not consider the direct current (DC) flowingthrough the interface. In 1968 [4], Geddes and

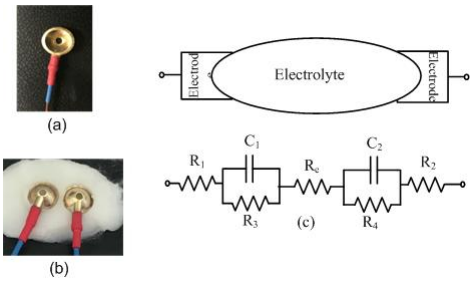

Figure 1.3. cup electrode (a) cup electrodes placed on Ten20 paste, (b) electrical circuit model of the electrode-electrolyte interface

Baker proposedanother model that considers the passage of DC through the interface. In theirmodel the Warburg capacitance is in parallel with the Faradic resistance to model the property of DC that passes through the interface. This model is shown in Fig. 1.2d.

Moreover, the exchange of the anions and cations at the interface alter the local concentration of cations and anions. Therefore, the neutrality of charge is altered in the solution and makes the electrolyte that is close to the interface a different potential with respect to the rest of the electrolyte, and causes an electric potential difference which is called the half-cell potential. The half-cell potential is related to the metal, the concentration of ions in the electrolyte, temperature and other second-order factors [2]. When a circuit is constructed to allow current to flow across an electrode-electrolyte interface, the observed half-cell potential is often altered. The difference between the observed half-cell potential for a particular circuit and the standard half-cell potential is known as the overpotential. Three basic mechanisms contribute to the overpotential: ohmic, concentration, and activation [2].

Electroencephalography (EEG) is an essential tool for brain and behavioral research. EEG is also one of the mainstays of hospital diagnostic procedures and presurgical planning. End users struggle with EEGs poor spatial resolution, selectivity and low signal-to-noise ratio, limiting its effectiveness in research discovery and diagnosis [5]-[6].

Tripolar concentric ring electrodes (TCREs), consisting of three elements including

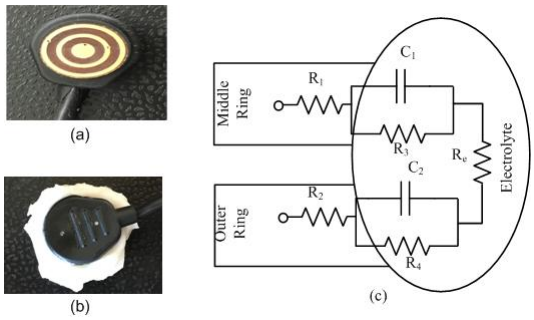

Figure 1.4. TCRE electrode (a) TCRE placed on Ten20 paste, (b) electrical circuit model of the electrode-electrolyte interface

the outer ring, the middle ring, and the central disc (Fig. 1.4a, b), are distinctively different from conventional disc electrodes that have a single element (Fig. 1.3a, b). TCREs have been shown to estimate the surface Laplacian directly [7]. The Laplacian algorithm is two-dimensional and weights the middle ring and central disc signal difference sixteen times greater than the outer ring and central disc signal difference [7]. Compared to EEG with conventional disc electrodes Laplacian EEG using TCREs (tEEG) have been shown to have significantly better spatial selectivity (approximately 2.5 times higher), signal-to-noise ratio (approximately 3.7 times higher), and mutual information (approximately 12 times lower) [8]. In this paper, we developed models for bio-potential electrodes. In particular, we developed mathematical models of our gold-plated TCRE and conventional golden plate cup electrode to compare their propertiesfor biomedical measurements.

1.2 Procedure

Fig. 1.3a illustrates a conventional cup electrode. In order to measure the impedance between two cup electrodes, fresh Ten20 (Weaver and Company) electrode paste was used in each experiment as a skin-to-electrode electrolyte, similar as in real recordings, and to mimic the body. Fig. 1.3b shows the cup electrodes placed in the Ten20 paste. The equivalent model for this configuration is shown in Fig. 1.3c. In this

model R1 and R2 represent the resistivity of the electrodes and C1 and C2 are the equivalent double layer capacitor of the electrode-electrolyte interface. The Re represents the electrolyte resistance, and the resistances R3 and R4 are the equivalent resistors for the leakage current of the electrode electrolyte interface.

Fig. 1.4a shows the TCRE andwith the electrolyte which is depicted in Fig. 1.4b. Therefore, there is anelectrode-electrolyte interface between each pair of rings of the TCRE. Fig. 1.4c shows part of theelectrical model representation for the TCRE electrode-electrolyte interface. (e.g. Middle and Outer elements of the TCRE).The impedance that is seen between the middle ring to the outer ring (Zmo) is:

$$Z_{mo} = R_1 + \frac{1}{j\omega C_1} + R_e + \frac{1}{j\omega C_2} + R_2 \tag{1.5}$$

and the resistive part is:

$$R_{mo} = R_1 + R_e + R_2 \tag{1.6}$$

where R_e is an ionic solution resistance that depends on the ionic concentration, types of the ions, temperature and the area in which current is carried. This resistance is defined as:

$$R_e = \rho \frac{L}{A} \tag{1.7}$$

where ρ is the solution resistivity. In biomedical applications, it is more common to use the conductivity of the solution. Since the solution conductivity, κ, is the reciprocal of the solution resistivity, ρ, we can formulate the solution conductivity, κ as:

$$\kappa = \frac{L}{RA} \tag{1.8}$$

and the reactive part is:

$$\frac{1}{C_{OD}} = \frac{1}{C_1} + \frac{1}{c_2} \tag{1.9}$$

Further, to measure the impedance, we performed electrochemical impedance spectroscopy (EIS) using the Gamry potentiostatic instrument framework. We configured the

system for two-electrode measurements. In order to measure the impedance between the central disc and middle ring (D-M), we connected the blue (working sense) and green (working current) leads to the middle ring and the white (reference) and red (counter current) leads to the central disc. To measure the impedance between the central disc and outer ring (D-O), we connected the blue and green leads to the outer ring and white and red leads to the central disc. Finally, to measure the impedance between the middlering and outer ring (M-O), we connected the blue and green leads to the middle ring and the white and red leads to the central disc. The same configuration was used for disc electrodes.

1.3 Results

Equation 5 shows that the impedance consists of capacitance and resistance. Therefore, the impedance changes with the frequency. The Bode plots of the impedances between each pair of rings (D-M, D-O, M-O) of TCRE are shown in Fig. 1.5a and their Nyquist plots are shown in Fig. 1.5b. The Bode and Nyquist plots for the cup electrodes are shown in Fig. 1.6. At low frequencies the cup electrode is more capacitive while the TCRE has a higher impedance in all frequencies. Based on the experimental results and the model parameters studied above, a proposed model for each pair of the tri-polar concentric ring electrode is depicted on Fig. 1.7.

In order to test the equivalent circuit model, a non-linear least squares fitting program was used to fit the model to the experimental data. The resulting fit with the experimental data for the impedance between the middle and outer rings is depicted in Fig. 1.5c and Fig 1.5d, and the parameter values are summarized in Table 1. For aperfect match of the model with the experimental data, a constant phase element (CPE) was used instead of capacitors. This is due to the"double layer capacitors" often behaves like a CPE instead of a pure capacitor [9], [10]. The impedance of a double layer capacitor

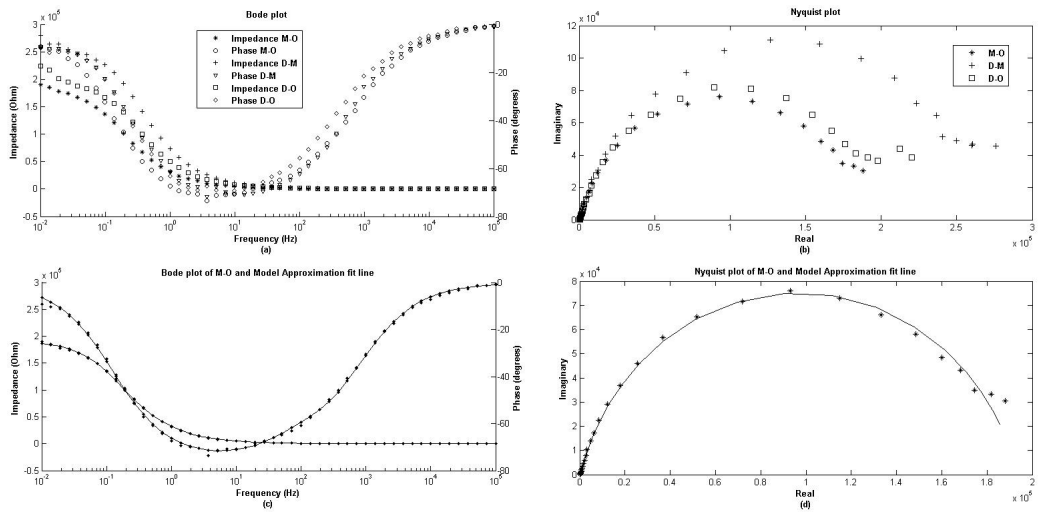

Figure 1.5. Bode plot of the TCRE (a), Nyquist plot of the TCRE (b), Bode plot of the TCRE with the fitted model (d), Nyquist plot of the TCRE with the fitted model

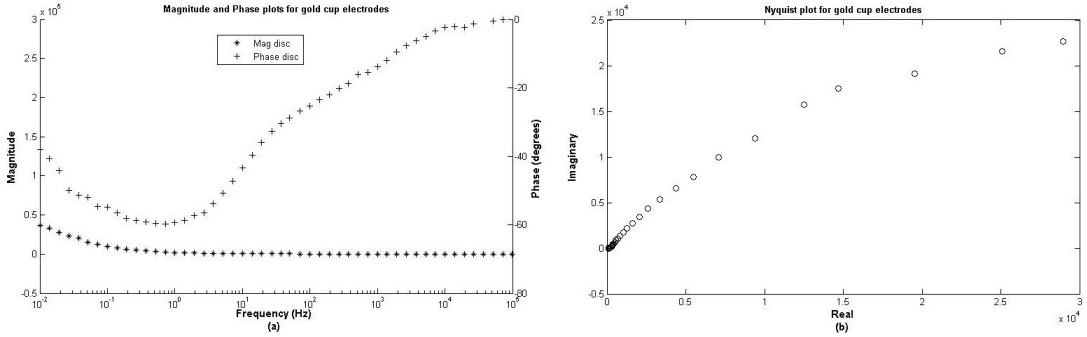

Figure 1.6. Bode plot of the cup electrode (a), Nyquist plot of the cup electrode (b)

has the form:

$$\frac{Z}{CPE} = \frac{1}{Q}(j\omega)^a \tag{1.10}$$

In equation 10, if the constant =1, the equation describes capacitance and has units of capacitance. Otherwise, if 0¡¡1, the equation represent the CPE and Q has units of $Fcm^{-}2s^{(}\alpha-1)$, $\frac{s^{\alpha}}{\Omega}$, $S.S^{\alpha}$. In Table 1 n and m correspond to the constant value of the CPE that is used for the Cw and Cd respectively.

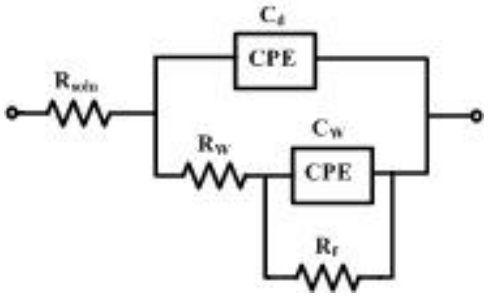

Figure 1.7. Bode plot of the cup electrode (a), Nyquist plot of the cup electrode (b)

Table 1.1. Parameter values for the tEEG model

Parameters	**TCRE (DM) 1020 Paste**	**TCRE (DO) 1020 Paste**	**TCRE (DM) TD-246 Paste**
Rsoln (ohms)	397.4 ± 3.501	435.3 ± 3.897	$2.37e+03 \pm 23.62$
Rcor (ohms)	$2.03e+05 \pm 4.94e+04$	$4.17e+05 \pm 1.55e+05$	$1.82e+07 \pm 1.62e+09$
Rpo (ohms)	$5.40e+05 \pm 3.14e+04$	$3.15e+05 \pm 1.24e+05$	$9.86e+05 \pm 9.47e+05$
Ccor $(\frac{s^\alpha}{\Omega})$	$2.16e-05 \pm 1.09e-05$	$2.93e-06 \pm 2.05e-06$	$3.73e-06 \pm 8.19e-06$
n	1.00 ± 1.66	$6.26e-01 \pm 1.58e-01$	$2.55e-01 \pm 1.03$
Cc $(\frac{s^\alpha}{\Omega})$	$2.87e-06 \pm 4.89e-08$	$3.06e-06 \pm 1.06e-07$	$1.10e-06 \pm 4.47e-08$
m	$8.70e-01 \pm 3.41e-03$	$8.68e-01 \pm 5.91e-03$	$7.53e-01 \pm 6.49e-03$

1.4 Conclusion

In this paper, a circuit model for the TCRE and electrode paste was developed and compared to a model for conventional disc electrodes. Observing Figures 1.5 and 1.6 there are two items to notice: (1) the TCRE phase only varies from 70 to 60 degrees in the frequency band 1Hz to 100Hz while the cup electrode phase varies from 60 to 25 degrees; and (2) the impedance of the TCRE is below $5k\Omega$ from 10Hz and beyond whereas the cup electrode impedance is below $5k\Omega$ beyond 0.5 Hz.

Acknowledgment

We would like to thank Dr. Richard Brown for allowing us to use the Gamry potentiostatic instrument framework machine.

[9, 10].

List of References

[1] L. A. Geddes, *Principles of applied biomedical instrumentation*. John Wiley & Sons, 1968.

[2] C. Boccaletti, F. Castrica, G. Fabbri, and M. Santello, "A non-invasive biopotential electrode for the correct detection of bioelectrical currents," in *Proceedings of the Sixth IASTED International Conference on Biomedical Engineering*. ACTA Press, 2008, pp. 353–358.

[3] H. Wang and L. Pilon, "Accurate simulations of electric double layer capacitance of ultramicroelectrodes," *The Journal of Physical Chemistry C*, vol. 115, no. 33, pp. 16 711–16 719, 2011.

[4] L. Geddes, "Historical evolution of circuit models for the electrode-electrolyte interface," *Annals of biomedical engineering*, vol. 25, no. 1, p. 1, 1997.

[5] J. E. Desmedt, V. Chalklin, and C. Tomberg, "Emulation of somatosensory evoked potential (sep) components with the 3-shell head model and the problem of ghost potential fields when using an average reference in brain mapping," *Electroencephalography and Clinical Neurophysiology/Evoked Potentials Section*, vol. 77, no. 4, pp. 243–258, 1990.

[6] P. Nunez, R. Silberstein, P. Cadusch, R. Wijesinghe, A. Westdorp, and R. Srinivasan, "A theoretical and experimental study of high resolution eeg based on surface laplacians and cortical imaging," *Electroencephalography and clinical neurophysiology*, vol. 90, no. 1, pp. 40–57, 1994.

[7] G. Besio, K. Koka, R. Aakula, and W. Dai, "Tri-polar concentric ring electrode development for laplacian electroencephalography," *IEEE transactions on biomedical engineering*, vol. 53, no. 5, pp. 926–933, 2006.

[8] K. Koka and W. G. Besio, "Improvement of spatial selectivity and decrease of mutual information of tri-polar concentric ring electrodes," *Journal of neuroscience methods*, vol. 165, no. 2, pp. 216–222, 2007.

[9] K. L. Turabian, *A Manual for Writers of Term Papers, Theses, and Dissertations, 6th. edn.* Chicago, Illinois, United States of America: University of Chicago Press, 1987.

[10] University of Rhode Island. “A guide to producing your thesis with latex.” June 2006. [Online]. Available: http://www.ele.uri.edu/info/thesis/guide

MANUSCRIPT 2

Impedance Spectroscopy of Tripolar Concentric Ring Electrodes with Ten20 and TD246 Pastes

Seyed Hadi Nasrollaholhosseini[1], Daniel Salazar Herrera[1], Walter G. Besio[1]

Published in the proceedings of the Engineering in Medicine and Biology Society (EMBC), 2017.

[1] Electrical, Computer, and Biomedical Engineering Department, University of Rhode Island, Kingston, RI 02881 USA.

abstract

Electrodes are used to transform ionic currents to electrical currents in biological systems. Modeling the electrode-electrolyte interface could help to optimize the performance of the electrode interface to achieve higher signal to noise ratios. There are previous reports of accurate models for single-element biomedical electrodes. In this paper, we measured the impedance on both tripolar concentric ring electrodes and standard cup electrodes by electrochemical impedance spectroscopy (EIS) using both Ten20 and TD246 electrode paste. Furthermore, we applied the model to prove that the model can predict the performance of the electrode-electrolyte interface for tripolar concentric ring electrodes (TCRE) that are used to record brain signals.

2.1 INTRODUCTION

Physiological systems such as cardiovascular system, nervous system, and muscular system all generate ionic current flows in the body. Each physiological process is associated with specific signals that reflect the underlying nature and activities of each source. One such physiological signal of interest is the electroencephalography (EEG) which is the recording of brain electrical activity. Brian signals, like other biomedical signals, can be obtained with electrodes that sense the variations in electrical potential generated by physiological processes. Electrodes convert the ionic currents flowing in the body generated by underlying cells into electrical currents [1]. Therefore, we need to understand the mechanisms that generate the transduction process between the electrode and human body. Equivalent circuit models of the electrode, electrolyte, and body may help us to have a better understanding of how biomedical signals are obtained by electrodes.

At the contact site of an electrode to the body an electrode-electrolyte interface forms. The contact of an electrode to electrolyte is depicted in Fig. 2.1. At the interface of electrode-electrolyte, chemical reactions take place that can be shown by the

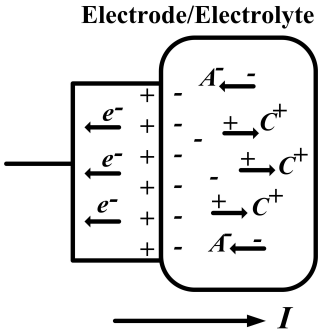

Figure 2.1. Electrode-Electrolyte Interface

following equations [2]:

$$C \Leftrightarrow C^{n+} + ne^{-} \tag{2.1}$$

$$A^{m-} \Leftrightarrow A + me^{-} \tag{2.2}$$

Obtaining an accurate model for the electrode-electrolyte interface is complicated and has been studied for many years. First, Helmholtz in 1879, proposed the concept of electric double layer [3]. He realized that at the electrode-electrolyte interface, since the electrolyte is saturated with charged electrons, the ions with the same charges will be pushed back while the opposite charges will be attracted. Therefore, at the electrode-electrolyte interface there will be two compact layers of opposite charges called the electric double layer (EDL). Warburg, in 1899, proposed a series combination of a capacitor and resistor in which the magnitude of the reactance and resistance is dependent on the electrode type, area (including surface conduction), electrolyte, frequency, and the current density [4]. In 1932 Fricke proposed a similar model for the electrode-electrolyte interface with the Warburg combination of series resistor and capacitor, adding that $C_W = \frac{K}{\omega^m}$ (k and m depend on the metal species) which reveals the frequency dependants of the capacitance. In 1947 Randles suggested another popular model that include a double-layer capacitance in parallel with a series combination of resistance and capacitance. In 1968 [1], Geddes and Baker proposed another model that considers the

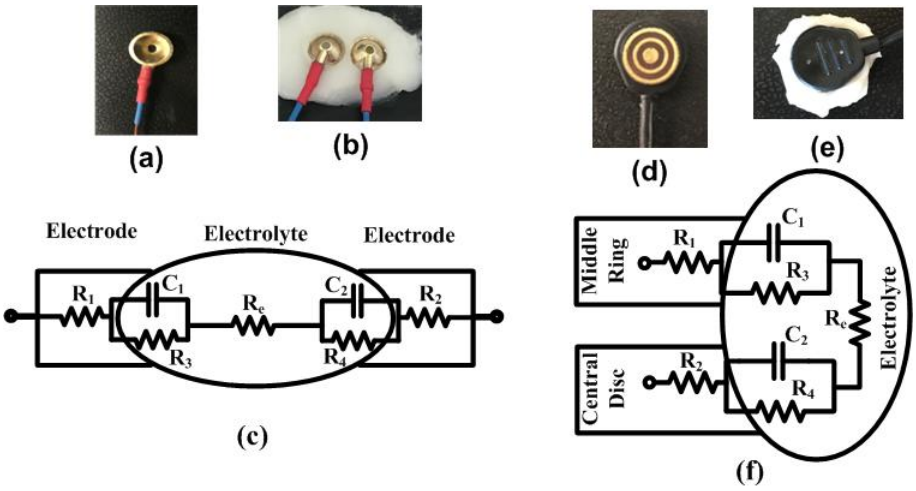

Figure 2.2. Cup electrode (a), cup electrodes placed on Ten20 paste (b), electrical circuit model of the cup electrode placed on an electrolyte (c), TCRE electrode (d) TCRE placed on Ten20 paste (e), electrical circuit model of the TCRE placed on an electrolyte (f)

passage of DC through the interface. In their model the Warburg capacitance is in parallel with the Faradic resistance to model the property of DC that passes through the interface. In [5], the author proposed a circuit model for the tripolar concentric ring electrode and compared the model with the conventional cup electrode. Their model is shown in Fig. 2.3 and is described in section II.

In this paper, we measured the impedance on both tripolar concentric ring electrodes and standard cup electrodes by electrochemical impedance spectroscopy (EIS) using both Ten20 and TD246 electrode paste. Furthermore, we applied the model that is proposed in [5] to prove that the model can predict the performance of the electrode.

The rest of the paper is organized as follows. The equivalent circuit model for the tripolar concentric ring electrode is explained in section II. The procedure of the measurement is addressed in section III. Section IV presents the results concluded by section V.

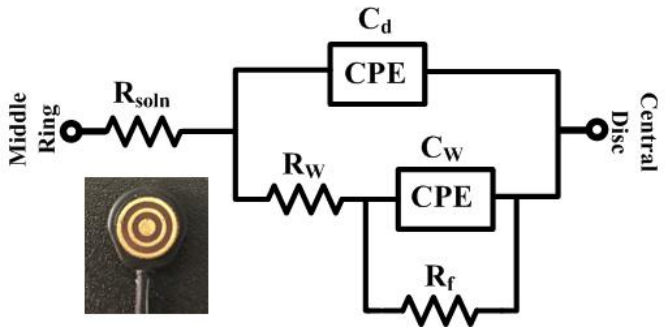

Figure 2.3. Electrical model for the tri-polar concentric ring electrode

2.2 Equivalent Circuit Model

Electroencephalography (EEG) is one of the mainstays of hospital diagnostic procedures and pre-surgical planning. End users struggle with EEGs poor spatial resolution, selectivity and low signal-to-noise ratio, limiting its effectiveness in research discovery and diagnosis [6]-[7]. Tripolar concentric ring electrodes (TCREs), consisting of three elements including the outer ring (inner radius is 4.4mm and outer radius is 5mm), the middle ring (inner radius is 2.5mm and outer radius is 3.2mm), and the central disc (radius is 1.4mm) (Fig. 2.2d, e), are distinctively different from conventional cup electrodes that have a single element (Fig. 2.2a, b). TCREs have been shown to estimate the surface Laplacian directly [8]. The Laplacian algorithm is two-dimensional and weights the middle ring and central disc signal difference sixteen times greater than the outer ring and central disc signal difference [9]. Compared to EEG with conventional cup electrodes Laplacian EEG using TCREs (tEEG) have been shown to have significantly better spatial selectivity (approximately 2.5 times higher), signal-to-noise ratio (approximately 3.7 times higher), and mutual information (approximately 12 times lower) [10].

Fig. 2.2a illustrates a conventional cup electrode. Fig. 2.2b shows the cup electrodes placed in the fresh Ten20 (Weaver and Company) paste as a skin-to-electrode electrolyte, similar as in real recordings, to mimic the body. The equivalent circuit model for this configuration is shown in Fig. 2.2c. TCRE electrode is also depicted in

Fig. 2.2d, and Fig. 2.2e shows the TCRE electrode is placed in fresh Ten20 paste. Therefore, there is an electrode-electrolyte interface between each pair of rings of the TCRE. Fig. 2.2f illustrates part of the electrical model representation for the TCRE electrode-electrolyte interface between the central disc and middle ring. In both models R_1, C_1 and R_2, C_2 are the equivalent series resistances and capacitances of the two electrode-electrolyte interfaces. The R_e represents the electrolyte resistance, and the resistances R_3 and R_4 are the equivalent resistances for the leakage current of the electrode-electrolyte interface. Therefore, if we neglect R_3 and R_4 for simplicity, the impedance that is seen between the middle ring to the central disc Z_{DM} is:

$$Z_{DM} = R_1 + \frac{1}{j\omega C_1} + R_e + \frac{1}{j\omega C_2} + R_2 \tag{2.3}$$

And the resistive part is:

$$R_{DM} = R_1 + R_e + R_2 \tag{2.4}$$

where $R_e = \rho \frac{L}{A}$ is an ionic solution resistance that depends on the ionic concentration, types of the ions, temperature and the area in which current is carried, and ρ is the solution resistivity. And the reactive part is:

$$\frac{1}{C_{DM}} = \frac{1}{C_1} + \frac{1}{C_2} \tag{2.5}$$

Based on the above mentioned parameters, and with the aid of the non-linear least squares fitting program of the electrochemical impedance spectroscopy (EIS), the authors proposed in [5] a model for the TCREs that is depicted in Fig. 2.3. In this model, R_{soln} is the equivalent solution (electrolyte) resistance, C_d represents the equivalent double layer capacitance, R_W and C_W are the equivalent Warburg combination, and R_f represents the equivalent leakage current in the electrode-electrolyte interface. For a perfect match of the model with the experimental data, a constant phase element (CPE) was used instead of capacitors. This is due to the ”double layer capacitors” often behaves like a

CPE instead of a pure capacitor [11], [12]. The impedance of a double layer capacitor has the form:

$$Z_{CPE} = \frac{1}{Q(j\omega)^{\alpha}} \tag{2.6}$$

In (6), if the constant $\alpha = 1$, the equation describes capacitance and Q has units of capacitance. Otherwise, if $0 < \alpha < 1$, the equation represent the CPE and Q has units of $Fcm^{-2}s^{(\alpha-1)}$, $\frac{s^{\alpha}}{\Omega}$.

2.3 Procedure

In order to measure impedances on both TCREs and standard cup electrodes, we performed electrochemical impedance spectroscopy (EIS) ten times each, using both Ten20 (Weaver Company) and TD-246 (Florida Research Instruments) electrode pastes. Both pastes are meant to serve as skin-to-electrode electrolytes, however the difference between the two is in their viscosity, and furthermore in their application. The Ten20 paste has a higher viscosity and therefore can be directly applied to the head with an electrode attached. Meanwhile, the TD-246 paste is much less viscous and requires the use of an electrode cap to assist in the adhesion of the electrode to the paste on the head. For our experiments we applied the paste on to a plastic plate and attached the electrodes directly to the paste in order to mimic the skin-to-electrode contact. To perform EIS measurements with both of these electrode pastes, we used the Gamrypotentiostatic instrument framework. The system was configured in order to perform two-electrode measurements. This allowed us to measure the impedances between the middle ring and central disc (M-D) of the TCRE?s, as well as the impedances between the outer ring and central disc (O-D). We also measured the impedances between two standard cup electrodes as reference. When measuring the impedance between middle ring and central disc we connected the blue (working sense) and green (working current) leads to the middle ring and the white (reference) and red (counter current) leads to the central disc. The same setup was used while measuring impedance between the outer ring and

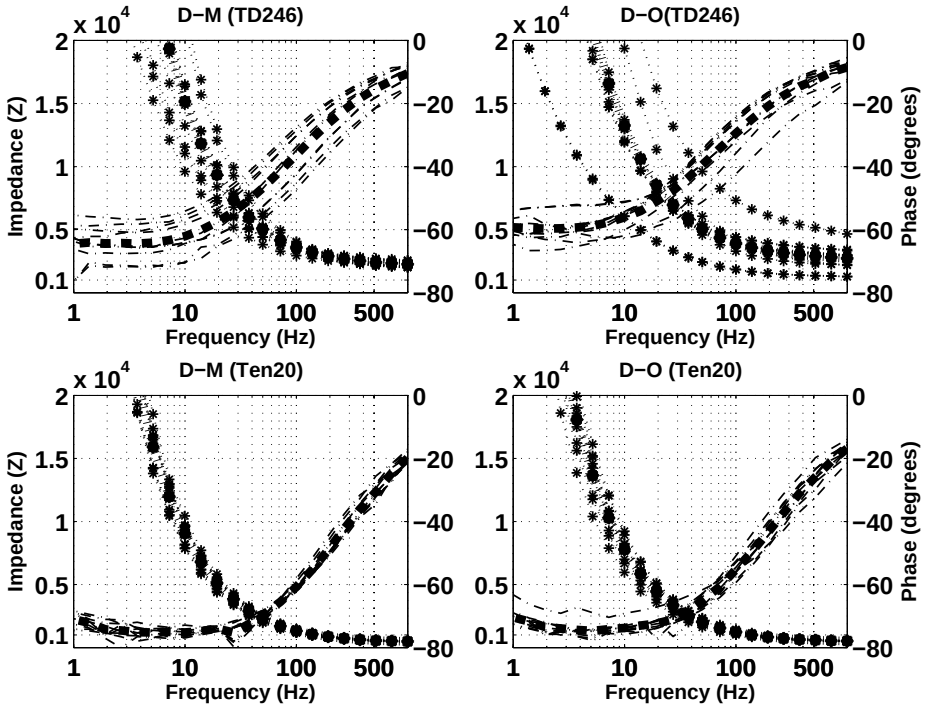

Figure 2.4. Bode plots of TCRE, central disc to outer ring (D-O) and central disc to middle ring (D-M) with Ten20 and TD246 pastes (10 experiments with average of them that the averaged in each graph is shown in bold) (asterisks are the impedance and phases are shown with dashed lines).

central disc, the only difference is the blue and green leads were now connected to the outer ring. The two standard cup electrodes were also connected in the same manner, with no specification as to which one went to green and blue leads or white and red leads. These were placed as close together on the same span of paste in order to resemble the measurements with the TCRE.

2.4 Results

The Bode plots for the TCRE between the central disc to middle ring (D-M) and the central disc to outer ring (D-O) using both Ten20 and TD246 paste are shown in Fig. 2.4. In each setup 10 experiments were run in order to reduce nuisance variables such as environmental noise. The bold line in the Bode plots represents the average of the ten

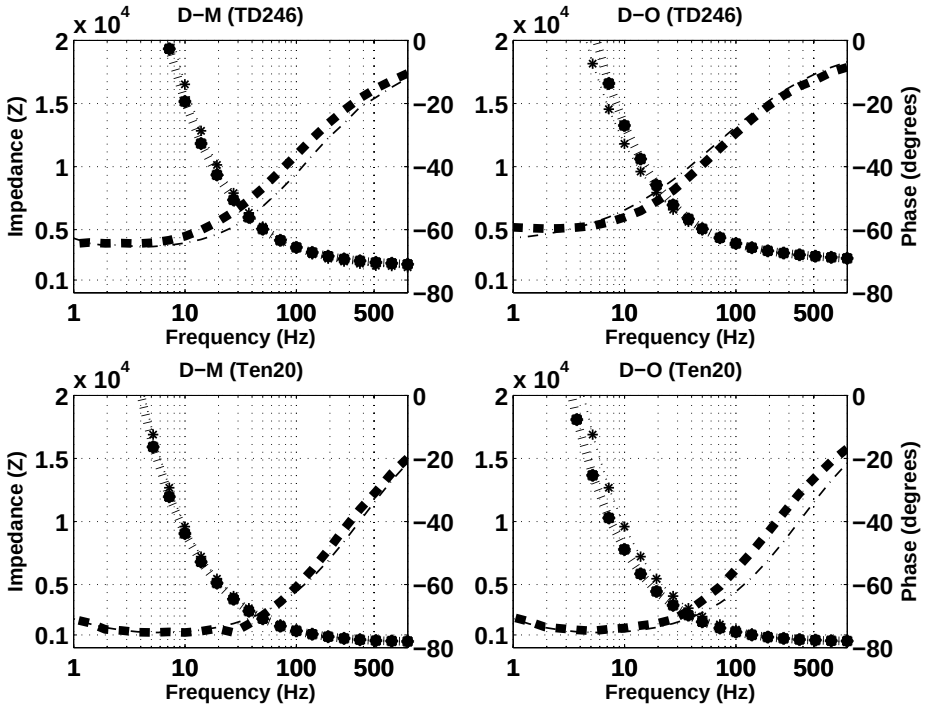

Figure 2.5. The averaged impedance and phase with the fit curves with the model for TCRE, central disc to outer ring (D-O) and central disc to middle ring (D-M) with Ten20 and TD246 pastes (averaged in each graph is shown in bold) (asterisks are the impedance and phases are shown with dashed lines).

experiments. The linear curve fits from the model, of impedances for the TCRE (D-M) rings and TCRE (D-O) rings are shown in Fig. 2.5, as well as the averaged curves. The model that is shown in Fig. 2.3 is used for the linear fit curves. As Fig. 2.5 shows, the fit curve matches the averaged curve. Therefore, the model in Fig. 2.3 can predict the performance of the TCRE.

Fig. 2.6 shows the standard cup electrode Bode plots using both Ten20 and TD-246 paste. Observing Fig. 2.4, 2.5 and 2.6 there are two items to notice: (1) the TCRE phase only varies from 70 to 60 degrees with the Ten20 paste and 40 to 60 with TD246 paste in the frequency band $1Hz$ to $100Hz$ while the cup electrode phase varies from 50 to 10 degrees with both Ten20 and TD-246; and (2) the impedance of the TCRE is below $5k\Omega$ from $10Hz$ and beyond with the Ten20 and is below $10k\Omega$ with TD246 whereas the cup

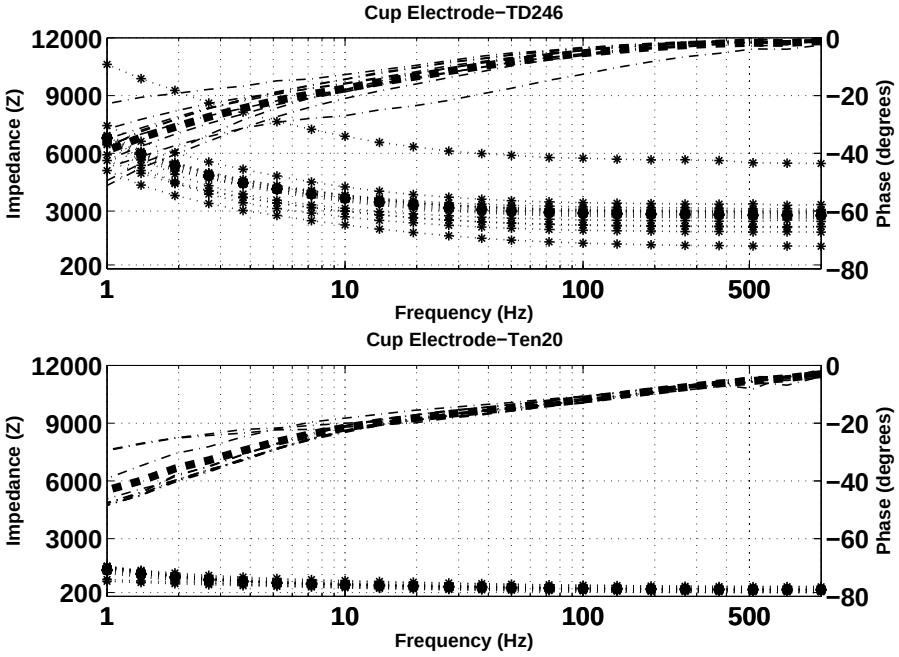

Figure 2.6. Bode plots of conventional cup electrode with Ten20 and TD246 pastes (10 experiments with average of them that the averaged in each graph is shown in bold) (asterisks are the impedance and phases are shown with dashed lines).

electrode impedance is below $6k\Omega$ beyond $1Hz$ for TD-246 and is below $1k\Omega$ beyond $1Hz$ for the Ten20.

Table 1 shows the parameter values of the equivalent circuit model that is depicted in Fig. 2.3 for the TCRE (D-O) rings, TCRE (D-M) rings, and standard cup electrodes using both Ten20 and TD246 paste. With the Ten20 paste the parameter values R_{soln}, R_{po}, n, and m were similar in all models (TCRE, (D-M), TCRE (D-O), and standard cup electrodes). However, the R_{soln}, C_{cor}, and C_c parameter values were higher in the TCRE models than the standard cup electrode models. With the TD246 paste the R_{soln}, R_{po}, n, and m parameter values were similar across all models. The R_{cor} value for the TCRE (D-O) model was similar to the standard cup electrode, but the value for the TCRE (D-M) model was higher than that of the standard cup electrode. Lastly the R_{po} parameter value was higher among both TCRE models than the standard cup electrode model.

Table 2.1. Parameter values for the tEEG model

Parameters	TCRE (DM) 1020 Paste	TCRE (DO) 1020 Paste	TCRE (DM) TD-246 Paste	TCRE (DO) TD-246 Paste	Standard Disc 1020 Paste	Standard Disc TD-246 Paste
Rsoln (ohms)	397.4 ± 3.501	435.3 ± 3.897	$2.37e+03$ ± 23.62	$2.63e+03$ ± 23.61	353.4 ± 3.291	$2.15e+03$ ± 16.38
Rcor (ohms)	$2.03e+05$ $\pm 4.94e+04$	$4.17e+05$ $\pm 1.55e+05$	$1.82e+07$ $\pm 1.62e+09$	$1.89e+04$ $\pm 2.67e+13$	1.829 $\pm 1.22e+08$	$5.20e+05$ $\pm 1.02e+05$
Rpo (ohms)	$5.40e+05$ $\pm 3.14e+04$	$3.15e+05$ $\pm 1.24e+05$	$9.86e+05$ $\pm 9.47e+05$	$5.52e+06$ $\pm 5.96e+12$	$3.71e+05$ $\pm 1.21e+08$	$4.24e+03$ $\pm 1.98e+03$
Ccor $(\frac{s^\alpha}{\Omega})$	$2.16e-05$ $\pm 1.09e-05$	$2.93e-06$ $\pm 2.05e-06$	$3.73e-06$ $\pm 8.19e-06$	$1.00e-04$ $\pm 6.52e+04$	$1.11e-01$ $\pm 1.14e+07$	$2.21e-05$ $\pm 8.39e-06$
n	1.00 ± 1.66	$6.26e-01$ $\pm 1.58e-01$	$2.55e-01$ ± 1.03	$6.36e-03$ $\pm 7.65e+06$	$5.44e-01$ $\pm 1.76e+06$	$8.63e-01$ $\pm 8.50e-02$
Cc $(\frac{s^\alpha}{\Omega})$	$2.87e-06$ $\pm 4.89e-08$	$3.06e-06$ $\pm 1.06e-07$	$1.10e-06$ $\pm 4.47e-08$	$4.67e-06$ $\pm 4.17e-07$	$2.11e-04$ $\pm 8.22e-05$	$3.32e-05$ $\pm 7.90e-06$
m	$8.70e-01$ $\pm 3.41e-03$	$8.68e-01$ $\pm 5.91e-03$	$7.53e-01$ $\pm 6.49e-03$	$7.29e-01$ $\pm 1.43e-02$	$6.67e-01$ $\pm 6.28e-02$	$7.36e-01$ $\pm 3.64e-02$

2.5 Conclusion

In conclusion, we find that our model can predict the compoents for different materails used for impedance matching. We also found that the impedances for the TD246 between the electrodes was higher than those for Ten20 paste. Furthermore, we found that the phase between two conventional disc electrodes varied more with frequency than the phase for the TCREs.

Acknowledgment

The authors would like to thank would like to thank Dr. Richard Brown for allowing us to use the Gamry potentiostatic instrument framework machine.

[13, 14].

List of References

[1] L. A. Geddes, *Principles of applied biomedical instrumentation*. John Wiley & Sons, 1968.

[2] C. Boccaletti, F. Castrica, G. Fabbri, and M. Santello, "A non-invasive biopotential electrode for the correct detection of bioelectrical currents," in *Proceedings of*

the Sixth IASTED International Conference on Biomedical Engineering. ACTA Press, 2008, pp. 353–358.

[3] H. Wang and L. Pilon, "Accurate simulations of electric double layer capacitance of ultramicroelectrodes," *The Journal of Physical Chemistry C*, vol. 115, no. 33, pp. 16 711–16 719, 2011.

[4] L. Geddes, "Historical evolution of circuit models for the electrode-electrolyte interface," *Annals of biomedical engineering*, vol. 25, no. 1, p. 1, 1997.

[5] S. H. Nasrollaholhosseini, P. Steele, and W. G. Besio, "Electrode-electrolyte interface model of tripolar concentric ring electrode and electrode paste," in *Engineering in Medicine and Biology Society (EMBC), 2016 IEEE 38th Annual International Conference of the*. IEEE, 2016, pp. 2071–2074.

[6] J. E. Desmedt, V. Chalklin, and C. Tomberg, "Emulation of somatosensory evoked potential (sep) components with the 3-shell head model and the problem of ghost potential fields when using an average reference in brain mapping," *Electroencephalography and Clinical Neurophysiology/Evoked Potentials Section*, vol. 77, no. 4, pp. 243–258, 1990.

[7] P. Nunez, R. Silberstein, P. Cadusch, R. Wijesinghe, A. Westdorp, and R. Srinivasan, "A theoretical and experimental study of high resolution eeg based on surface laplacians and cortical imaging," *Electroencephalography and clinical neurophysiology*, vol. 90, no. 1, pp. 40–57, 1994.

[8] G. Besio, K. Koka, R. Aakula, and W. Dai, "Tri-polar concentric ring electrode development for laplacian electroencephalography," *IEEE transactions on biomedical engineering*, vol. 53, no. 5, pp. 926–933, 2006.

[9] G. Besio, K. Koka, R. Aakula, and W. Dai, "Tri-polar concentric ring electrode development for laplacian electroencephalography," *IEEE transactions on biomedical engineering*, vol. 53, no. 5, pp. 926–933, 2006.

[10] K. Koka and W. G. Besio, "Improvement of spatial selectivity and decrease of mutual information of tri-polar concentric ring electrodes," *Journal of neuroscience methods*, vol. 165, no. 2, pp. 216–222, 2007.

[11] B. Hirschorn, M. E. Orazem, B. Tribollet, V. Vivier, I. Frateur, and M. Musiani, "Constant-phase-element behavior caused by resistivity distributions in films i. theory," *Journal of The Electrochemical Society*, vol. 157, no. 12, pp. C452–C457, 2010.

[12] J.-h. Chang, J. Park, Y. K. Pak, and J. J. Pak, "Fitting improvement using a new electrical circuit model for the electrode-electrolyte interface," in *Neural Engineering, 2007. CNE'07. 3rd International IEEE/EMBS Conference on*. IEEE, 2007, pp. 572–574.

[13] K. L. Turabian, *A Manual for Writers of Term Papers, Theses, and Dissertations, 6th. edn.* Chicago, Illinois, United States of America: University of Chicago Press, 1987.

[14] University of Rhode Island. “A guide to producing your thesis with latex.” June 2006. [Online]. Available: http://www.ele.uri.edu/info/thesis/guide

MANUSCRIPT 3

Electrode-Electrolyte Interface Modeling and Impedance Characterizing of Tripolar Concentric Ring Electrode

Seyed Hadi Nasrollaholhosseini[1], Jason Mercier[1], Godi Fischer[1], Walter G. Besio[1]

Under revision at the IEEE Transactions on Biomedical Engineering (TBME)

[1] Electrical, Computer, and Biomedical Engineering Department, University of Rhode Island, Kingston, RI 02881 USA.

abstract

Electrodes are used to convert ionic currents to electrical currents in biological systems. Modeling the electrode-electrolyte interface and characterizing the impedance of the interface could help to optimize the performance of the electrode interface to achieve higher signal to noise ratios. Previous work has yielded accurate models for single-element biomedical electrodes. This paper introduces a model for a tripolar concentric ring electrode (TCRE) derived from impedance measurements using electrochemical impedance spectroscopy (EIS) with a Ten20 electrode impedance matching paste. It is shown that the model serves well to predict the performance of the electrode-electrolyte interface for TCREs as well as standard cup electrodes. In this paper we also discuss the comparison between the TCRE and the standard cup electrode regarding their impedance characterization and demonstrate the benefit of using TCREs in biomedical applications. We have also conducted auditory evoked potential experiments using both TCRE and standard cup electrodes. The results show that EEG recorded from tripolar concentric ring electrodes (tEEG) is beneficial, acquiring the auditory brainstem response (ABR) with less stimuli with respect to recoding EEG using standard cup electrodes.

3.1 INTRODUCTION

Physiological systems such as the cardiovascular system, the nervous system, and the muscular system all generate ionic current flows in the body. Each physiological process is associated with specific signals that reflect the underlying nature and activities of each source. Biomedical signals can be obtained with electrodes that measure local electrical activities generated by physiological processes. One such biomedical signal of interest is the electroencephalography (EEG) signal revealing electrical activity of the brain.

The electrodes convert the ionic currents generated by the underlying cells of the

human body into electrical currents [1]. In essence, they act as transducers between ionic and electronic currents. A mathematical model of the electrode, electrolyte, and body may help us to have a better understanding of how electrodes record biomedical signals. Since electrodes act as transducers, we need to understand the mechanisms that generate the transduction process between the electrode and the human body. Moreover, physiological processes in the human body generate ionic current flows in the volume conductor, the body. Hence, an electrode-electrolyte interface forms the contact site of an electrode to the body. Figure 3.1 illustrates the contact of an electrode to an electrolyte. At the interface of electrode-electrolyte, chemical reactions take place that can be described by the following equations [2]:

$$C \Leftrightarrow C^{n+} + ne^{-} \tag{3.1}$$

$$A^{m-} \Leftrightarrow A + me^{-} \tag{3.2}$$

Equation (1) describes the oxidation reaction from left to right, and the reduction reaction from right to left, and both reduction and oxidation can occur at the electrode-electrolyte interface. It also reveals that for an efficient electron-ion exchange at the interface, we should place a metal (C) into an aqueous solution containing ions of the metal (C+). Thus, oxidation causes cations to be dispersed into the electrolyte and electrons to be left in the electrode. Equation (2) shows that the anions (A) can also be oxidized to a neutral atom and release one or more electrons by moving to the interface.

Obtaining an accurate model for the electrode-electrolyte interface is an on-going research topic, which has been studied for many years. The electric double layer (EDL) concept was first proposed by Helmholtz in 1879 [3]. He found that at the electrode-electrolyte interface, since the electrolyte is saturated with charged electrons, the coions will be pushed back while the counterions will be attracted. Therefore, there will be

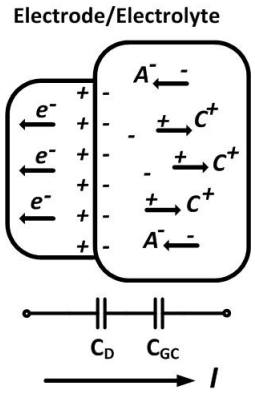

Figure 3.1. Electrode-Electrolyte Interface

two compact layers of opposite charges at the electrode-electrolyte interface called the electric double layer. More specifically, an electric double layer is obtained as a series combination of two conventional capacitors consisting of Helmholtz capacitance and the Gouy-Chapman capacitance that are shown in Fig. 3.1 as C_d and C_{GD} respectively and are discussed in detail in III "Equivalent Circuit Model".

Warburg was the first who proposed an electrode-electrolyte model in 1899. His proposed model consists of a series combination of a capacitor, C_W, and resistor, R_W which are shown in Fig. 3.2A. The reactance and resistance magnitudes are dependent on the electrode type, the area (including surface conduction), the electrolyte, the frequency, and the current density [4]. In the Warburg model R_ω and C_ω were proposed for an infinitely low density current, which decreases as the inverse square root of frequency $(\frac{1}{\sqrt{f}})$.

In 1932, Fricke, suggested a similar model for the electrode-electrolyte interface. He kept the Warburg combination of a series resistor and capacitor but added that $C_\omega = \frac{k}{\omega^m}$. In the Fricke model shown in Fig. 3.2b, the Warburg reactance and resistance become:

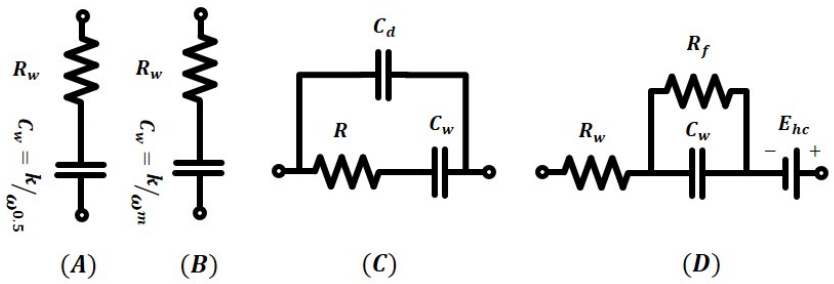

Figure 3.2. Electrical circuit model evolution of the electrode-electrolyte interface. (A) Warburg, (B) Fricke (C) Randles, and (D) Geddes and Baker models

$$X_\omega = \frac{1}{k\omega^{1-m}} \tag{3.3}$$

$$R_\omega = \frac{X_\omega}{\tan\frac{m\pi}{2}} \tag{3.4}$$

where k and m depend on the metal species.

Another popular model for the electrode-electrolyte interface was proposed by Randles in 1947 which is illustrated in Fig. 3.2C. In this model, a double-layer capacitance C_d was added in parallel with a series combination of resistance R and capacitance C. However, the above mentioned models do not consider the direct current (DC) flowing through the interface. In 1968 [4], Geddes and Baker proposed another model that included the passage of a DC current through the interface. In their model, the Warburg capacitance, C_W is connected in parallel with the Faradic resistance, R_f to model the property of DC current through the interface. This model is shown in Fig. 3.2D.

The exchange of the anions and cations at the interface alters the local concentration of cations and anions. Therefore, the neutrality of charge is altered in the solution. As a result, the electrolyte that is closest to the interface has a different potential with respect to the rest of the electrolyte. This electric potential difference is called the half-cell potential. The half-cell potential is related to the metal, the concentration of ions in the electrolyte, temperature and other second-order factors [2]. When a circuit is constructed to allow current to flow across an electrode-electrolyte interface, the observed

half-cell potential is often altered. The difference between the observed half-cell potential for a particular circuit and the standard half-cell potential is known as the overpotential. Three basic mechanisms contribute to the overpotential: ohmic, concentration, and activation [2].

Tripolar concentric ring electrodes (TCREs) consisting of an outer ring, a middle ring, and a central disc (Fig. 3.5D, 3.5E), are distinctively different from conventional cup electrodes featuring a single element (Fig. 3.5A, 3.5B). TCREs have been shown to reveal the local surface Laplacian directly, the second spatial derivative of the surface potentials [5], a two-dimensional Laplacian algorithm that weights the middle ring and central disc signal difference sixteen times greater than the outer ring and central disc difference [5]. Compared to EEG from conventional cup electrodes, tripolar Laplacian EEGs from TCREs (tEEG) have been shown to feature approximately 2.5 times higher spatial selectivity, 3.7 times higher signal-to noise ratio and about 12 times lower mutual information [6].

In this paper, we measured the impedance on both tripolar concentric ring electrodes and standard cup electrodes by electrochemical impedance spectroscopy (EIS) using the two electrode and three electrode experiments of the Gamry potentiostat. We also predicted the performance by utilizing the model proposed in [7], [8] and compared the theoretical results to the recordings.

The paper is organized as follows. Section II explains the procedure of how the impedance is measured using EIS. The equivalent circuit model for the tripolar concentric ring electrode is addressed in section III. Section IV presents the results and section V draws some conclusions.

3.2 Procedure

In order to measure impedances on both TCREs and standard cup electrodes, we performed electrochemical impedance spectroscopy (EIS) ten times each, using Ten20

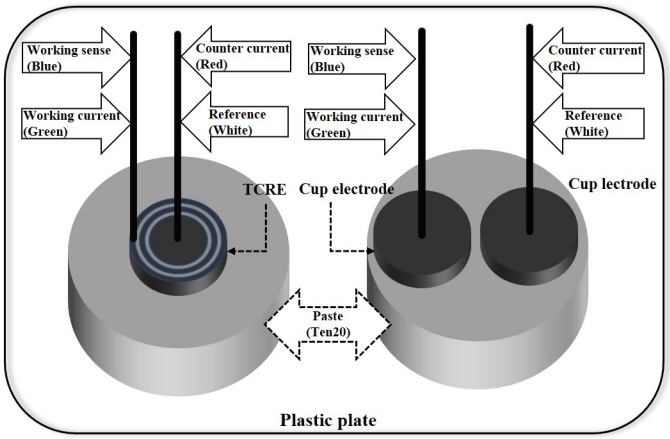

Figure 3.3. Two electrode setup of TCRE and conventional cup electrode

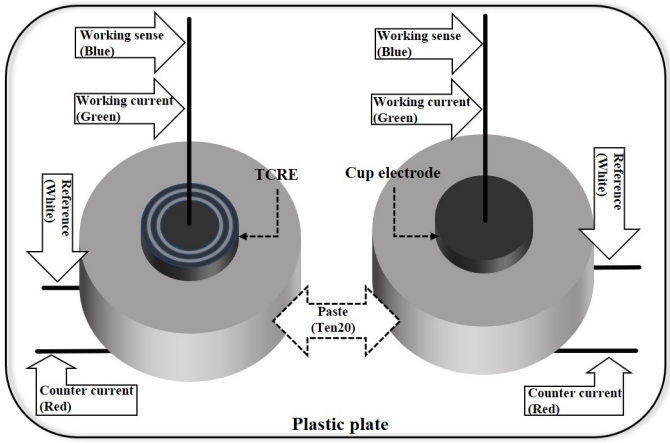

Figure 3.4. Three electrode setup of TCRE and conventional cup electrode

(Weaver Company) as an electrode paste. There is little agreement on the values of skull conductivity in the literature. Reports range from 0.2-0.53 S/m for the conductivity of the scalp in the literature [9]-[10]. We also measured the conductivity of the Ten-20 paste and found that it has a similar conductivity as the scalp, approximately 0.44 S/m. For our experiments we applied the paste on to a plastic plate and attached the electrodes directly to the paste in order to mimic the skin-to-electrode contact. To perform EIS measurements, we used the Gamry potentiostatic instrument framework. The system was configured in order to perform both two-electrode and Three-electrode measurements.

The Gamry potentiostat we used is a 4-probe instrument. This means there are four relevant leads that need to be placed. The two-electrode set up as depicted in Fig. 3.3) allowed us to measure the impedances between the middle ring and central disc (M-D) of the TCREs, as well as the impedances between the outer ring and central disc (O-D). When measuring the impedance between middle ring and central disc, we connected the blue (working sense) and green (working current) leads to the middle ring and the white (reference) and red (counter current) leads to the central disc. The same setup was used while measuring the impedance between outer ring and central disc, the only difference was the blue and green leads were now connected to the outer ring.

We utilized the three-electrode configuration to measure the impedance of each ring (the central disc, the middle ring and the outer ring) to the electrolyte (as shown in Fig. 3.4). In this set up, the white lead (reference) is separated from the red lead (counter). When measuring the impedance between the central disc and the electrolyte, the green and blue leads (working and working sense) are attached to the central disc. A copper 15 awg wire is connected to the white lead (reference) and is positioned so that it is measuring a point very close to the working and working sense electrodes. The same type of wire is connected to the red lead (counter) that is placed 1cm away in the paste. To measure the impedances of the middle ring to the electrolyte and the outer ring to the electrolyte, a similar configuration was used, except that the working, and the working sense, leads were now connected to the middle and the outer ring, respectively.

To obtain a reference, we also measured the impedances between two standard cup electrodes in a two electrode set up (as shown in Fig. 3.3) as well as between the standard cup electrode and the electrolyte in a three electrode configuration (as illustrated in Fig. 3.4). In the two electrode configuration, the two standard cup electrodes were connected in the same manner with no specification as to which one went to green and blue or white and red leads. The leads were placed as close together as possible on the same

span of paste in order to resemble the measurement conditions for the TCRE recordings. Furthermore, in the three electrode configuration, an analogous condition to the TCRE recording was used.

3.3 Equivalent Circuit Model

Electroencephalography (EEG) is one of the mainstays of hospital diagnostic procedures and pre-surgical planning. Unfortunately, end users frequently struggle with EEGs poor spatial resolution, selectivity and low signal-to-noise ratio, which limits its effectiveness in research, discovery and diagnosis [11]-[12]. Having an outer ring with 4.4mm inner radius, 5mm outer radius, a middle ring with 2.5mm inner radius and 3.2mm outer radius a central disc with 1.4mm radius (Fig. 3.5D, 3.5E) renders tripolar concentric ring electrodes (TCREs) distinctively different from conventional cup electrodes (Fig. 3.5A and 3.5B). However, the total diameter of both the TCRE and the cup electrode are 10mm and both are gold plated.

Fig. 3.5A illustrates a conventional cup electrode. Fig. 3.5B shows the cup electrodes placed in the fresh Ten20 (Weaver and Company) paste similar to real recordings

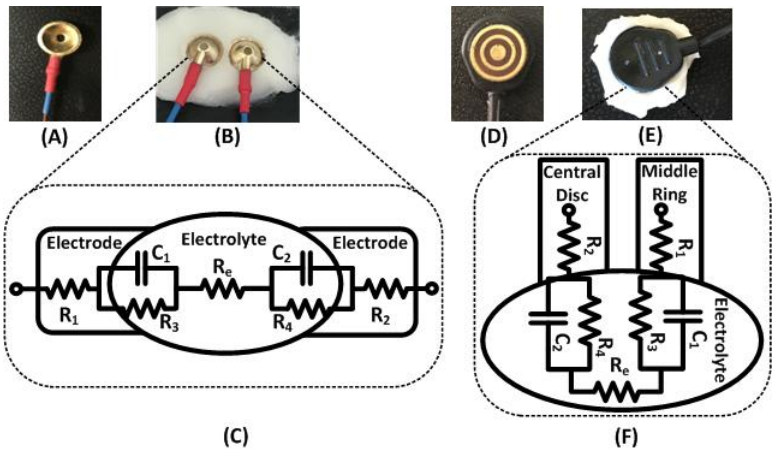

Figure 3.5. Disc electrode (A), Disc electrodes placed on Ten20 paste (B), electrical circuit model of the Disc electrode placed on the electrolyte (C), TCRE electrode (D) TCRE placed on Ten20 paste (E), electrical circuit model of the TCRE placed on the electrolyte (F)

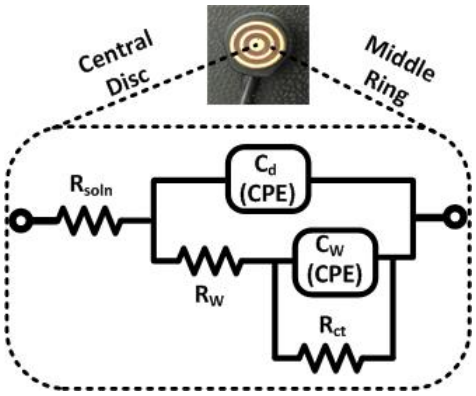

Figure 3.6. Electrical model for the tri-polar concentric ring electrode

to mimic the body. The equivalent circuit model for this configuration is shown in Fig. 3.5C. The TCRE electrode in Fig. 3.5E is placed in fresh Ten20 paste. Therefore, there is an electrode-electrolyte interface between each pair of rings of the TCRE. Fig. 3.5F illustrates part of the electrical model representation for the TCRE electrode-electrolyte interface between the central disc and middle ring. In both models, as presented above in Fig. 3.2, R_1, C_1 and R_2, C_2 are the equivalent series resistances and capacitances of the two electrode-electrolyte interfaces. For the TCRE, there will be two more such models: one for the outer ring and central disc, and one for the middle ring and outer ring. R_e represents the electrolyte resistance and the resistors R_3 and R_4 are the equivalent resistances for the leakage current of the electrode-electrolyte interface, respectively. Therefore, if we neglect R_3 and R_4 at higher frequency, the impedance seen between the middle ring to the central disc Z_{DM} becomes:

$$Z_{DM} = R_1 + \frac{1}{j\omega C_1} + R_e + \frac{1}{j\omega C_2} + R_2 \tag{3.5}$$

the resistive part in equation (5) is:

$$R_{DM} = R_1 + R_e + R_2 \tag{3.6}$$

where R_e is an ionic solution resistance, which depends on the ion concentration, ion

type, temperature and active cross section. The reactive part in equation (5) is:

$$\frac{1}{C_{DM}} = \frac{1}{C_1} + \frac{1}{C_2} \tag{3.7}$$

The authors proposed the TCRE model that is depicted in Fig. 3.6 [7]-[8]. A non-linear least squares fitting program was used to fit the model to the experimental data. The Simplex algorithm in the Echem Analyst was utilized for fitting. The algorithm automatically adjusts the parameter values of the elements in the model to find the best fit. In this model, R_{soln} is the equivalent solution (electrolyte) resistance, C_d represents the equivalent double layer capacitance, R_W and C_W are the equivalent Warburg combination and R_{ct} is the charge-transfer resistance, which represents the equivalent Faradic leakage process in the electrode-electrolyte interface according to [13], [14]:

$$R_{ct} = \frac{kT}{qzJ_0} \tag{3.8}$$

where k is the Boltzmann constant, T denotes the absolute temperature, q is the electron charge, z denotes the charge on the ion in solution and J_0 represents the equilibrium charge density.

The resistor R_{soln} in the proposed model dominates the impedance at high frequencies. This resistance encompasses all the paths from electrode to electrolyte such as: interconnect resistance and solution or spreading resistance. For a round electrode, its value is [13], [14], [15]:

$$R_{soln} = \frac{\rho}{4r} \tag{3.9}$$

where r and ρ represent the radius and the solution resistivity respectively.

To match the model perfectly with the experimental data, a constant phase element (CPE) was used instead of capacitors. In fact, double layer capacitors often behave like

CPEs rather than pure capacitors [16], [17]. The impedance of a double layer capacitor has the form:

$$Z_{CPE} = \frac{1}{Q(j\omega)^{\alpha}} \tag{3.10}$$

If $\alpha = 1$, this equation describes a capacitance and Q has units of Farad. If $0 < \alpha < 1$, the equation represent a CPE and Q has units of $Fcm^{-2}s^{(\alpha-1)}$, $\frac{s^{\alpha}}{\Omega}$.

An electric double layer is obtained as a series combination of two capacitances consisting of the Helmholtz capacitance and the Gouy-Chapman capacitance, which is a diffuse layer accounting for the mobility of ions in the electrolyte [3]. In order to relate the potential with the charge distribution, Poisson's equation is used to define the variation of potential (φ) with distance in the Helmholtz layer. Besides, if we assume a one dimensional potential variation in the direction perpendicular to the solid solution interface, we have [3], [13]-[18]:

$$\frac{d^2\varphi}{dx^2} = -\frac{\rho(x)}{\varepsilon_0 \varepsilon_r} \tag{3.11}$$

where (φ) is the electric potential, ρ is the charge density, ε_0 is the permittivity of free space, ε_r is the permittivity of the medium and x is the distance from the electrode.

If we consider ions as point charges in the Helmholtz layer, the capacitance per unit surface area of the Helmholtz double layer denoted by C_H becomes [3], [13]-[18]:

$$C_H = \frac{\varepsilon_0 \varepsilon_H}{d_H} \tag{3.12}$$

where ε_H is the relative permittivity of the Helmholtz plane and d_H the distance of the Helmholtz plane to the electrode. d_H can be approximated as the radius of solvated ions.

Gouy and Chapman modified the double layer electrode model, which is shown in Fig. 3.1 as C_{GC}, by also taking into account the mobility of ions in the solution.

An accumulation of oppositely charged ions will be outside the Helmholtz layer. The distribution of ions is given by the Boltzmann distribution [3]:

$$n_i = n_i^{\infty} exp(-\frac{z_i e\varphi}{kT}) \tag{3.13}$$

where n_i is the ions concentration of type i per unit volume near the interface, n_i^{∞} the concentration of ions of type i per unit volume in the bulk solution, e the electronic charge, z_i the charge on the ion i, k the Boltzmann constant and T the absolute temperature.

The total charge density per unit volume for all ionic species is given by the sum over all ions:

$$\rho = \sum_i z_i e n_i = \sum_i z_i e n_i^{\infty} exp(-\frac{z_i e\varphi}{kT}) \tag{3.14}$$

The Poisson-Boltzmann equation is obtained by combining equations (11) and (14):

$$\frac{d^2\varphi}{dx^2} = -\frac{e}{\varepsilon_0 \varepsilon_r} \sum_i z_i n_i^{\infty} exp(-\frac{z_i e\varphi}{kT}) \tag{3.15}$$

By multiplying both sides of equation (15) by $2\frac{dy}{dx}$, and solving for a planar electrode considering the boundary conditions: (1) $\varphi(0) = \varphi_0$ and (2) $\varphi(\infty) = 0$ and solved further for a symmetrical electrolyte yields:

$$\frac{d\varphi}{dx} = \sqrt{\frac{2kTn^{\infty}}{\varepsilon_r \varepsilon_0}} \left[exp(-\frac{ze\varphi_d}{2kT}) - exp(\frac{ze\varphi_d}{2kT}) \right] \tag{3.16}$$

If σ_d is the charge density of the diffused layer expressed in C/m^2 then,

$$\sigma_d = -\varepsilon_r \varepsilon_0 \frac{d\varphi}{dx} \mid_{x=0} \tag{3.17}$$

The charge density of the diffused layer can be derived from equations (16) and (17) and becomes,

$$\begin{aligned}\sigma_d &= -\varepsilon_r\varepsilon_0\frac{d\varphi}{dx}\,|_{x=0} \\ &= \sqrt{2kTn^{\infty}\varepsilon_r\varepsilon_0}\left[exp(\frac{ze\varphi_d}{2kT}) - exp(-\frac{ze\varphi_d}{2kT})\right] \\ &= \sqrt{8kTn^{\infty}\varepsilon_r\varepsilon_0}\,\sinh\left(\frac{ze\varphi_d}{2kT}\right)\end{aligned} \tag{3.18}$$

Finally, the differential Gouy-Chapman capacitance is obtained by differentiating equation (17) [3], [18],

$$C_{GC} = \frac{d\sigma_d}{d\varphi_0} = \sqrt{\frac{2z^2e^2n^{\infty}\varepsilon_r\varepsilon_0}{kT}}\,\cosh\left(\frac{ze\varphi_d}{2kT}\right) \tag{3.19}$$

Therefore, the double layer capacitance that occurs at the electrode-electrolyte interface is the series combination of the Helmholtz capacitance and the Gouy-Chapman capacitance. This combination model is given by Stern and is called "Gouy-Chapman-Stern" model and can be written as [3], [13]-[18]:

$$\frac{1}{C_{dl}} = \frac{1}{C_H} + \frac{1}{C_{GC}} \tag{3.20}$$

3.4 Auditory Evoked Potential

Evoked potentials are the brains electrical activity recorded in response to a stimulation of one of the bodys sensory mechanisms. The early component of the overall auditory evoked potential (AEP) is the auditory brain stem response (ABR) which can be recorded from the electrodes placed on the scalp of a subject [19]-[22]. The ABR has a very low amplitude. Therefore, to extract the ABR from background EEG, repeated trials are averaged synchronized to the stimulus. The averaging technique improves the signal-to-noise ratio of the ABR significantly. This technique employs about 2000-3000 responses which have the same time window to the stimulus [19]-[21]. Thus, signal averaging can be very time consuming and uncomfortable for both clinicians and subjects. Reducing the required number of trials would be of great signicance. In this test, a Brain Products V-Amp and Recorder software was used to record the tEEG and EEG signals

simultaneously with the sampling rate of 20,000 Hz. The intensity of the audio cue was adjusted to 70dB and a frequency of 4 kHz with a duration of 1.0 ms that was repeated at 39.1 Hz was provided. The participant listened to 100 consecutive audio cues followed by a rest pause and then repeated ten times for a total of 1000 audio cues.

The participant (n=6, 2 female) signed URI IRB approved consents and sat in a comfortable position in front of the computer screen and had TCREs placed at position C_z and the right mastoid, with a reference cup electrode placed on the left mastoid and a ground cup electrode placed on the mid-forehead. Audio cues were provided to the right ear with an earbud. Testing was performed in a quiet, but not soundshielded room, with eyes closed. During the breaks, participants could open their eyes and adjust their position if needed. The computer monitor showed a countdown clock of pending audio cues. The ABRs data for this study were bandpass filtered at 300-900 Hz (Butterworth forward and backward) and epoch windowed between -5 ms prior to, and up to 15 ms after the stimuli.

3.5 Results

EIS: The Bode plots resulting from the two electrode set up for the TCRE between central disc to middle ring (DM) and central disc to outer ring (DO) using the Ten20 paste are shown in Fig. 3.7 and Fig. 3.8, respectively. Figures 3.9-3.11 depict the Bode plots measuring the impedances of each ring (central disc, middle and outer ring) to the electrolyte utilizing three electrode configuration. In each setup, 10 experiments were conducted in order to reduce nuisance variables such as environmental noise. In each figure, the top plot shows the results of 10 different experiments in which the average of these ten experiments is represented in bold. Moreover, the bottom plot in each figure shows the linear curve fits derived from the model for the TCRE that is shown with a dashed bold trace as well as the averaged curves that are plotted with a solid trace. Besides, in each figure, the impedance curves are specified with squares. The model

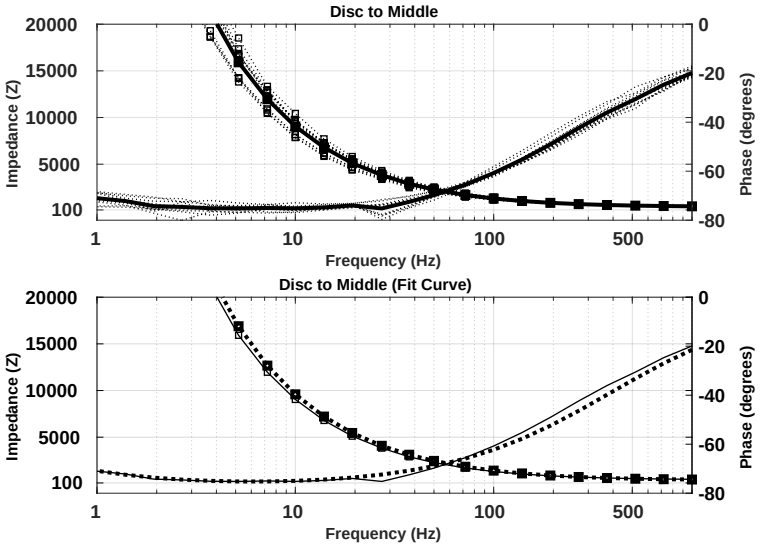

Figure 3.7. Bode plots of the TCRE for the central disc to middle ring (D-M) with Ten20 paste. Impedance is specified with squares. The average of the 10 experiments is shown with the bold trace (top). The fit curve is shown with a dashed bold trace and the averaged data is shown with a solid trace (bottom).

illustrated in Fig. 3.6 was used for the linear curve fit. It can be seen from Fig. 3.7 through Fig. 3.11 that the fitted curve matches the averaged curve at the interested frequency range of 1Hz to 1kHz very well. Therefore, the model in Fig. 3.6 can predict the performance of the TCRE accurately.

Figure 3.12 shows the standard cup electrode Bode plots using the two electrode set up and the same Ten20 paste. The results for the standard cup electrode using the three electrode set up are depicted in Fig. 3.13. In each case, the top plot shows the ten experiments with the average in bold as well as the linear curve fit using the model of Fig. 3.6 with the averaged curve in the bottom plot. It can also be deduced from Fig. 3.12 and Fig. 3.13 that the model of Fig. 3.6 predicts the behavior of the standard cup electrode equally well.

When inspecting Fig. 3.7, through Fig. 3.13, we notice: (1) the TCRE phase only changes from -70 to -60 degrees with the Ten20 paste in the frequency band $1Hz$ to $100Hz$ while the standard cup electrode phase varies from -75 to -35 degrees. This

Table 3.1. Parameter values for the tEEG model

Parameters	TCRE (Disc to Middle)	TCRE (Disc to Outer)	TCRE (Disc to Electrolyte)	TCRE (Middle to Electrolyte)	TCRE (Outer to Electrolyte)	Standard Disc to Standard Disc	Standard Disc to Electrolyte
$\mathbf{R_{soln}}(\Omega)$	397.4 ± 3.501	435.3 ± 3.897	292.6 ± 2.21	179.4 ± 1.72	204.6 ± 1.5	351.9 ± 2.69	110.2 ± 1.16
$\mathbf{R_{ct}}(\Omega)$	$2.03e+5$ $\pm 4.94e+4$	$4.17e+5$ $\pm 1.55e+5$	$119.3e+3$ $\pm 235.9e+3$	$98.84e+3$ $\pm 5.04e+3$	$49.56e+3$ $\pm 17.41e+3$	$95.34e+3$ $\pm 6.66e+3$	$23.67e+3$ $\pm 1.45e+3$
$\mathbf{R_w}(\Omega)$	$5.40e+05$ $\pm 3.14e+04$	$3.15e+05$ $\pm 1.24e+05$	$179e+3$ $\pm 23.67e+3$	$112.6e+3$ $\pm 166.5e+2$	$49.29e+3$ $\pm 8.35e+3$	$1.079e+3$ ± 662.5	214.3 ± 339.4
$\mathbf{C_w}(\frac{s^\alpha}{\Omega})$	$2.16e-05$ $\pm 1.09e-05$	$2.93e-06$ $\pm 2.05e-06$	$14.62e-6$ $\pm 4.5e-6$	$8.96e-6$ $\pm 3.7e-6$	$10.9e-6$ $\pm 2.2e-6$	$1.61e-6$ $\pm 1.26e-6$	$23.65e-6$ $\pm 40.1e-6$
$\alpha_\mathbf{W}$	1.00 ± 1.66	$6.26e-01$ $\pm 1.58e-01$	1.0 $\pm 629.8e-3$	$745.1e-3$ $\pm 84.7e-3$	$911.5e-3$ $\pm 196.8e-3$	1.00 $\pm 103.8e-3$	$808.5e-3$ $\pm 135.9e-3$
$\mathbf{C_d}(\frac{s^\alpha}{\Omega})$	$2.87e-06$ $\pm 4.89e-08$	$3.06e-06$ $\pm 1.06e-07$	$5.191e-6$ $\pm 125.9e-9$	$2.421e-6$ $\pm 3.9e-9$	$8.24e-6$ $\pm 287.6e-9$	$832.4e-3$ $\pm 10.43e-3$	$843.8e-3$ $\pm 127.5e-3$
$\alpha_\mathbf{d}$	$8.70e-01$ $\pm 3.41e-03$	$8.68e-01$ $\pm 5.91e-03$	$848.2e-3$ $\pm 4.3e-3$	1.0 $\pm 155.2e-3$	$877.4e-3$ $\pm 5.95e-3$	$832.4e-3$ $\pm 10.43e-3$	$843.8e-3$ $\pm 127.5e-3$

shows that TCREs are more robust for phase analysis. (2) the impedance values between the TCRE electrodes are generally higher than between two standard cup electrodes. They are below $10k\Omega$ only from $10Hz$ and beyond, whereas the standard cup electrode impedance is below $5k\Omega$ beyond $3Hz$. (3) The impedance of the centeral disc to elec-

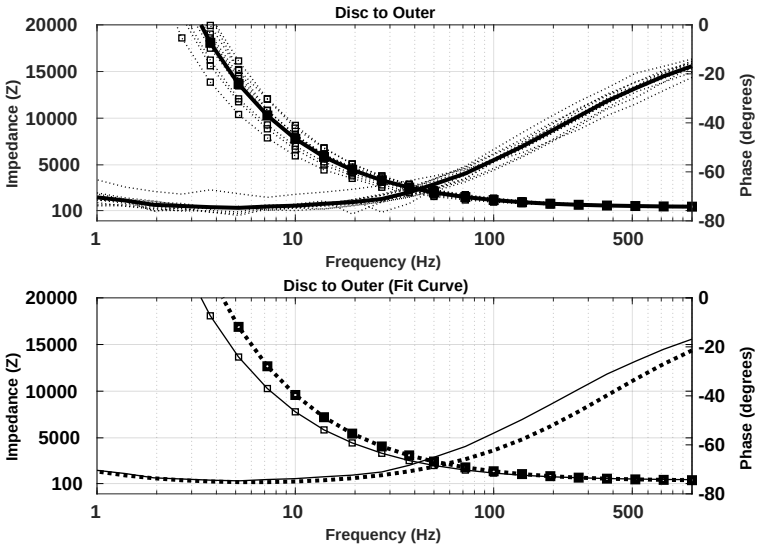

Figure 3.8. Bode plots of the TCRE for the central disc to outer ring (D-O) with Ten20 paste. Impedance is specified with squares. The average of the 10 experiments is shown with the bold trace (top). The fit curve is shown with a dashed bold trace and the averaged data is shown with a solid trace (bottom).

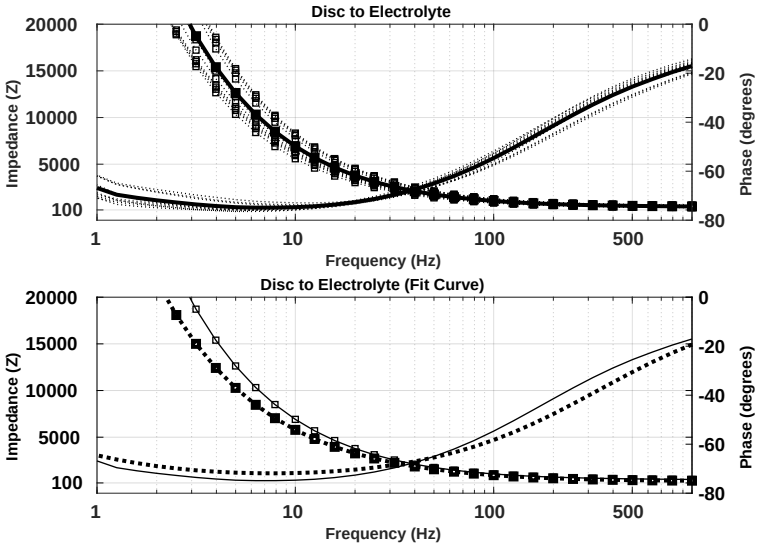

Figure 3.9. Bode plots of the TCRE for the central disc to electrolyte (Ten20 paste). Impedance is specified with squares. The average of the 10 experiments is shown with the bold trace (top). The fit curve is shown with a dashed bold trace and the averaged data is shown with a solid trace (bottom).

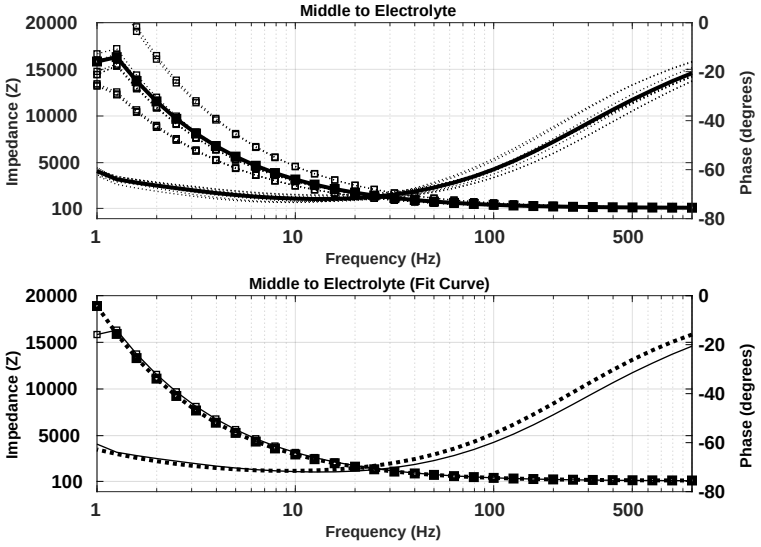

Figure 3.10. Bode plots of the TCRE for the middle ring to electrolyte (Ten20 paste). Impedance is specified with squares. The average of the 10 experiments is shown with the bold trace (top). The fit curve is shown with a dashed bold trace and the averaged data is shown with a solid trace (bottom).

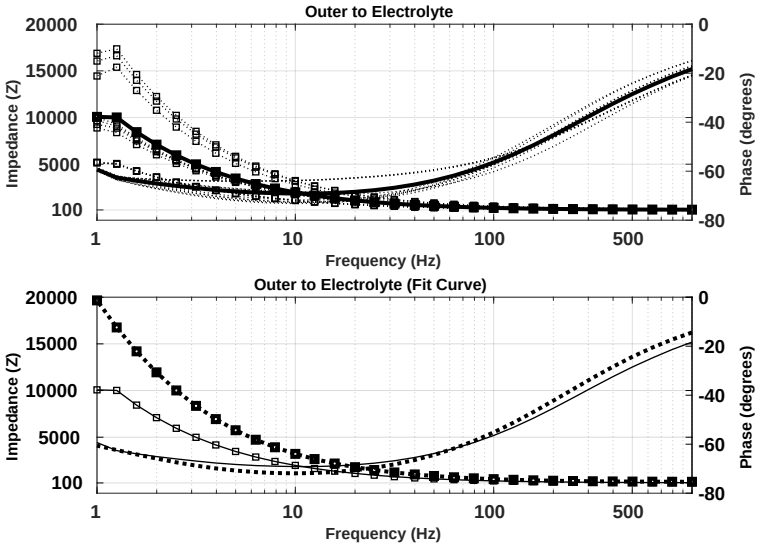

Figure 3.11. Bode plots of the TCRE for the outer ring to electrolyte (Ten20 paste). Impedance is specified with squares. The average of the 10 experiments is shown with the bold trace (top). The fit curve is shown with a dashed bold trace and the averaged data is shown with a solid trace (bottom).

trolyte is greater than the impedance between middle ring to electrolyte and outer ring to electrolyte. Furthermore, the impedance of the middle ring to electrolyte is greater than the outer ring to electrolyte impedance. (4) the impedance between each ring to electrolyte is smaller than the impedances between central disc to middle and central disc to outer ring in the frequency range $1Hz$ to $100Hz$. This shows that the three rings of the TCREs are not shorted in this frequency range. (5) the impedance between cup electrode to electrolyte is smaller than the impedances between two cup electrodes. Table 1 lists the averaged, fitted parameter values of the equivalent circuit model depicted in Fig. 3.6 with the corresponding standard deviations for disc to middle ring, disc to outer ring, disc, middle, and outer rings to electrolyte as well as standard cup electrode to standard cup electrode and standard cup electrode to electrolyte using the Ten20 paste. C_W and C_d are representing the constant phase elements that are used instead of conventional capacitances in the model of Fig. 3.6 to match the model perfectly with the experimental data. In Table I if the α_W and α_d are 1 the unit of C_W and C_d, as it is described in

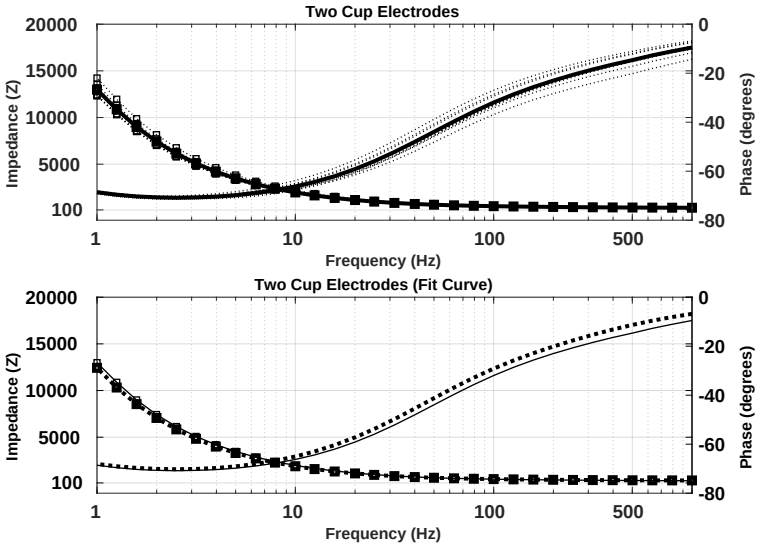

Figure 3.12. Bode plots between two conventional cup electrode with electrolyte (Ten20 paste). Impedance is specified with squares. The average of the 10 experiments is shown with the bold trace (top). The fit curve is shown with a dashed bold trace and the averaged data is shown with a solid trace (bottom).

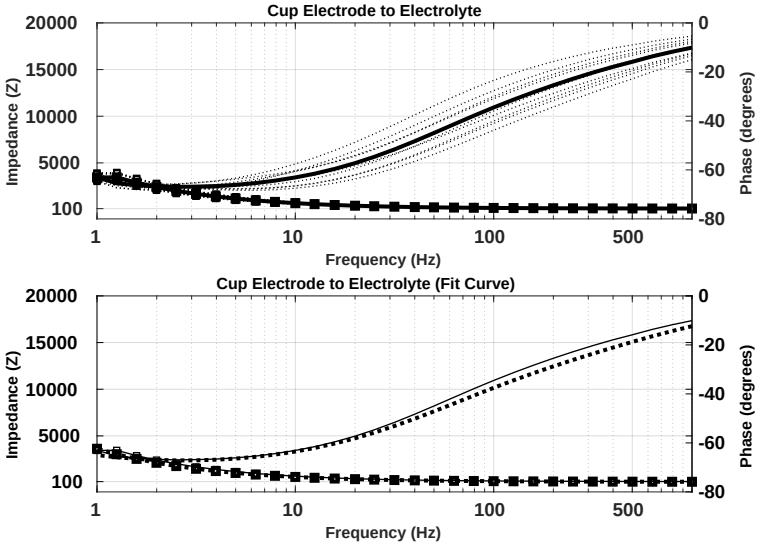

Figure 3.13. Bode plots of the conventional cup electrode to electrolyte (Ten20 paste). Impedance is specified with squares. The average of the 10 experiments is shown with the bold trace (top). The fit curve is shown with a dashed bold trace and the averaged data is shown with a solid trace (bottom).

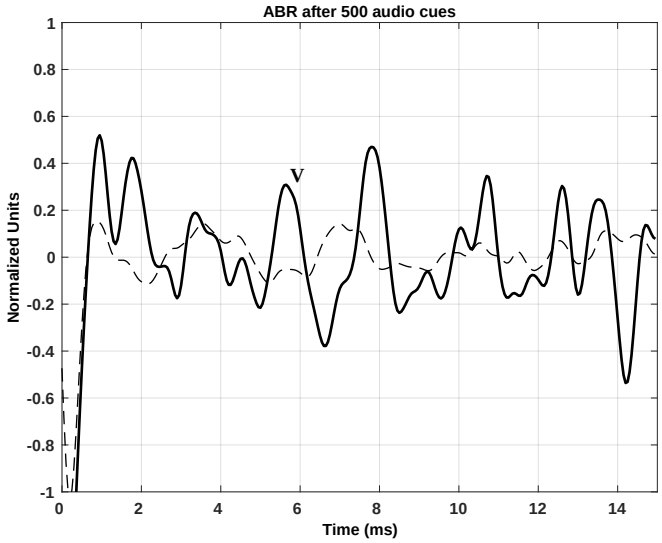

Figure 3.14. tEEG (solid bolded traces) vs. EEG (dotted trace) after 500 audio cues.

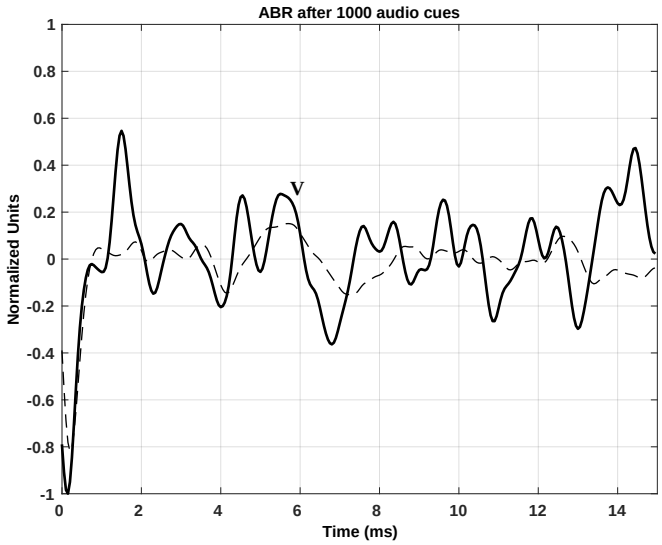

Figure 3.15. tEEG (solid bolded traces) vs. EEG (dotted trace) after 1000 audio cues.

equation 10, are in F, and the value would be as described in equation 20. With the paste, the parameter values R_{soln}, n, and m were similar for TCREs. The standard deviation for R_{soln}, n, and m, C_d are less than 10% in almost all cases. However, in some cases the variation for R_w, R_{ct}, and C_w, C_d are higher. This might be due to the sensitivity of these parameters with regard to the electrode-electrolyte interface condition.

ABR: The participants all tolerated the experiment. Wave V latency consistently revealed ABR responses at varying stimulation rates and is widely used to detect and mark auditory brainstem responses [19]-[21]. It has been shown that the wave V is identified as the peak near 6 ms after the stimulus onset and immediately before the negative slope [19]-[21]. Wave V has been attributed to activity in the lateral lemniscus and inferior colliculus. Fig. 3.14 depicts the ABR of the tEEG and EEG with 500 stimuli. Most of the ABR waves are becoming evident in the tEEG (solid trace), although not fully defined. It is not possible to tell if there is an ABR response in the EEG (dash-dotted trace). In Figure 3.15, after 1000 auditory stimuli, the ABR waves are well defined for the tEEG (solid bold trace). However, even after 1000 auditory stimuli there still is no evident ABR waves in the EEG (dash-dotted trace).

3.6 Conclusion

The goal of this study was to use EIS to enhance our understanding of the physical processes determining the electrode-electrolyte interface with a focus on TCREs and to find an appropriate model, which can be used to improve the interface design. EIS has been utilized to analyze the behavior of the TCRE and the cup electrode, and an equivalent circuit model was used to describe and quantify the electrode-electrolyte interface impedance. The good match between the experimental results and fitted curves derived from an equivalent circuit model shows that the model predicts the behavior of the TCREs very well. Moreover, equations are presented to describe the physical process of the electrode-electrolyte interface. We found that the impedance between the electrodes of the TCREs decreases less with frequency than the impedance between the electrodes to the Ten20 paste. The impedance between the two cup electrodes is so low that it prevents high spatial resolution since it almost shorts the circuit out. We also found that the phase of the TCRE is flatter from 1 to 100 Hz than the phase of the cup electrode. This would be beneficial when conducting a phase analysis.

Equations 3-4, 8-10, 12, 20 in section III, showed the relationship of the electrode parameters to the electrode type, the area, the electrolyte, the frequency and the current density. This is also proven by the experimental data shown in Figures 3.7-3.13. For the TCRE, the central disc has the lowest surface area and the plot in Fig. 3.9 depicts that it has the highest impedance compared to the middle and outer rings. On the other hand, the outer ring has the highest surface area, and the plot in Fig. 3.11 illustrates that it has the lowest impedance. Moreover, since the cup electrode has larger surface area than the elements of the TCRE, the plot in Figures 3.12-3.13 shows that it has less impedance than the TCRE. The proposed model of Fig. 3.6 depicts that at higher frequencies the impedance of the double layer capacitor, C_d, becomes so small and shorts the part of the model in parallel to it. However, the model shows that the impedance between the rings would be limited to R_{soln}. The value of the R_{soln}, as shown in Table I, is about 300Ω at approximately $1kHz$, not a short.

Furthermore, our experiment showed that the response in the ABR can be detected reliably with only 500 stimuli by using tripolar concentric ring electrodes. The standard number of stimuli is 2000 to detect the ABR by conventional electrode signal averaging [19]-[21]. In particular, for hearing screening of newborns the number of stimuli should be kept to a minimum. Therefore, detecting the ABR by fewer trials offers a great advantage of TCREs. If only the wave V is needed, then it is likely possible to complete the hearing test using tEEG with 500, or less, audio stimuli.

Acknowledgment

The authors would like to thank Dr. Richard Brown for allowing us to use the Gamry potentiostatic instrument framework machine.

[23, 24].

List of References

[1] L. A. Geddes and L. E. Baker, *Principles of applied biomedical instrumentation*. John Wiley & Sons, 1989.

[2] C. Boccaletti, F. Castrica, G. Fabbri, and M. Santello, "A non-invasive biopotential electrode for the correct detection of bioelectrical currents," in *Proceedings of the Sixth IASTED International Conference on Biomedical Engineering*. ACTA Press, 2008, pp. 353–358.

[3] H. Wang and L. Pilon, "Accurate simulations of electric double layer capacitance of ultramicroelectrodes," *The Journal of Physical Chemistry C*, vol. 115, no. 33, pp. 16 711–16 719, 2011.

[4] L. Geddes, "Historical evolution of circuit models for the electrode-electrolyte interface," *Annals of biomedical engineering*, vol. 25, no. 1, p. 1, 1997.

[5] G. Besio, K. Koka, R. Aakula, and W. Dai, "Tri-polar concentric ring electrode development for laplacian electroencephalography," *IEEE transactions on biomedical engineering*, vol. 53, no. 5, pp. 926–933, 2006.

[6] K. Koka and W. G. Besio, "Improvement of spatial selectivity and decrease of mutual information of tri-polar concentric ring electrodes," *Journal of neuroscience methods*, vol. 165, no. 2, pp. 216–222, 2007.

[7] S. H. Nasrollaholhosseini, P. Steele, and W. G. Besio, "Electrode-electrolyte interface model of tripolar concentric ring electrode and electrode paste," in *Engineering in Medicine and Biology Society (EMBC), 2016 IEEE 38th Annual International Conference of the*. IEEE, 2016, pp. 2071–2074.

[8] S. H. Nasrollaholhosseini, D. S. Herrera, and W. G. Besio, "Impedance spectroscopy of tripolar concentric ring electrodes with ten20 and td246 pastes," in *Engineering in Medicine and Biology Society (EMBC), 2017 39th Annual International Conference of the IEEE*. IEEE, 2017, pp. 2426–2429.

[9] M. Fernández-Corazza, S. Turovets, P. Luu, N. Price, C. H. Muravchik, and D. Tucker, "Skull modeling effects in conductivity estimates using parametric electrical impedance tomography," *IEEE Transactions on Biomedical Engineering*, vol. 65, no. 8, pp. 1785–1797, 2018.

[10] T. F. Oostendorp, J. Delbeke, and D. F. Stegeman, "The conductivity of the human skull: results of in vivo and in vitro measurements," *IEEE transactions on biomedical engineering*, vol. 47, no. 11, pp. 1487–1492, 2000.

[11] J. E. Desmedt, V. Chalklin, and C. Tomberg, "Emulation of somatosensory evoked potential (sep) components with the 3-shell head model and the problem of ghost

potential fields when using an average reference in brain mapping," *Electroencephalography and Clinical Neurophysiology/Evoked Potentials Section*, vol. 77, no. 4, pp. 243–258, 1990.

[12] P. Nunez, R. Silberstein, P. Cadusch, R. Wijesinghe, A. Westdorp, and R. Srinivasan, "A theoretical and experimental study of high resolution eeg based on surface laplacians and cortical imaging," *Electroencephalography and clinical neurophysiology*, vol. 90, no. 1, pp. 40–57, 1994.

[13] N. Joye, A. Schmid, and Y. Leblebici, "Electrical modeling of the cell–electrode interface for recording neural activity from high-density microelectrode arrays," *Neurocomputing*, vol. 73, no. 1-3, pp. 250–259, 2009.

[14] W. Franks, I. Schenker, P. Schmutz, and A. Hierlemann, "Impedance characterization and modeling of electrodes for biomedical applications," *IEEE Transactions on Biomedical Engineering*, vol. 52, no. 7, pp. 1295–1302, 2005.

[15] T. Jochum, T. Denison, and P. Wolf, "Integrated circuit amplifiers for multi-electrode intracortical recording," *Journal of neural engineering*, vol. 6, no. 1, p. 012001, 2009.

[16] B. Hirschorn, M. E. Orazem, B. Tribollet, V. Vivier, I. Frateur, and M. Musiani, "Constant-phase-element behavior caused by resistivity distributions in films i. theory," *Journal of The Electrochemical Society*, vol. 157, no. 12, pp. C452–C457, 2010.

[17] J.-h. Chang, J. Park, Y. K. Pak, and J. J. Pak, "Fitting improvement using a new electrical circuit model for the electrode-electrolyte interface," in *Neural Engineering, 2007. CNE'07. 3rd International IEEE/EMBS Conference on*. IEEE, 2007, pp. 572–574.

[18] E. Gongadze, S. Petersen, U. Beck, and U. van Rienen, "Classical models of the interface between an electrode and an electrolyte," in *COMSOL Conference*, 2009, pp. 14–16.

[19] R. Zhang, G. McAllister, B. Scotney, S. McClean, and G. Houston, "Combining wavelet analysis and bayesian networks for the classification of auditory brainstem response," *IEEE Transactions on Information Technology in Biomedicine*, vol. 10, no. 3, pp. 458–467, 2006.

[20] C. N. Rocha-Muniz, D. M. Befi-Lopes, and E. Schochat, "Investigation of auditory processing disorder and language impairment using the speech-evoked auditory brainstem response," *Hearing research*, vol. 294, no. 1-2, pp. 143–152, 2012.

[21] J. Krizman, E. Skoe, and N. Kraus, "Stimulus rate and subcortical auditory processing of speech," *Audiology and Neurotology*, vol. 15, no. 5, pp. 332–342, 2010.

[22] J. H. Kim, I. Song, S. M. Lee, H. S. Choi, H. Byeon, I. Kim, and S.-H. Lee, "An electroplating-free and minimal noise polyimide microelectrode for recording auditory evoked potentials from the epicranius," *IEEE Transactions on Biomedical Engineering*, vol. 60, no. 12, pp. 3425–3431, 2013.

[23] K. L. Turabian, *A Manual for Writers of Term Papers, Theses, and Dissertations, 6th. edn.* Chicago, Illinois, United States of America: University of Chicago Press, 1987.

[24] University of Rhode Island. "A guide to producing your thesis with latex." June 2006. [Online]. Available: http://www.ele.uri.edu/info/thesis/guide

MANUSCRIPT 4

Digital Tripolar Concentric Ring Electrode for Biopotential Signal Recordings

Seyed Hadi Nasrollaholhosseini[1], Godi Fischer[1], Walter G. Besio[1]

In Preparation for submission at the IEEE Transaction on Biomedical Circuits and Systems (TBioCAS)

[1] Electrical, Computer, and Biomedical Engineering Department, University of Rhode Island, Kingston, RI 02881 USA.

abstract

Ubiquitous physiological monitoring will be a key driving force in the upcoming medical revolution. Cardiac and brain signals in the form of electrocardiogram (ECG) and electroencephalogram (EEG) are two critical health indicators that directly benefit from long-term monitoring. The tripolar concentric ring electrode (TCRE) has proved to be sensitive enough to visualize electrical impulses that correspond to a persons specific thoughts patterns. In past TCRE applications, the electrode outputs have been fed to the pre-amplifiers via coax cables. To circumvent this rather costly solution and simplify the data transfer, we have realized an active TCRE, which digitizes the sensitive electrode signals at the front end. The digital outputs are then sent to a host computer in serial format for further processing. The digital electrode would form an ideal building block for electrode arrays, since the single-bit outputs can readily be time-multiplexed onto one or multiple high-speed data channels adjusted for array size.

4.1 INTRODUCTION

The U.S. has 12.3% disabled people based on the 2012 American Community Survey (ACS). According to this survey, more than half of the disabled population has ambulatory disability. Therefore, a system which enables people with disabilities to control their environment is crucially important. Moreover, ubiquitous physiological monitoring will be a key driving force in the upcoming medical revolution.

Physiological systems such as the cardiovascular system, the nervous system and the muscular system generate ionic current flows in the body. Each physiological process is associated with specific signals that reflect the underlying nature and activities of each source. Physiological recordings of interest are electrocardiograms (ECGs) and electroencephalographs (EEGs), signals reflecting the status of the heart and the electrical activities of the brain, respectively.

Brain-computer interfaces (BCIs) are systems that can detect patterns in brain sig-

nals related to human intentions, more specifically, they translate intention into a control signal to communicate between the brain and the external world such as a computer. BCI systems have the potential to substantially increase and improve the quality-of-life of people suffering from severe motor disabilities including paralysis, and provide a new way for able-bodied people to control computers or other devices (e.g., a robot arm, an artificial limb or a computer cursor). The most important clinical applications of BCI systems include brain-derived communication in paralyzed and locked-in patients and restoration of motor function in patients with spinal cord injuries. BCIs enable users to control devices with direct brain communication using the electroencephalographic activity recorded by electrodes placed on the scalp (non-invasive BCI) or with single-neuron activity recorded within the brain (Invasive BCI). Invasive BCIs face substantial technical difficulties and clinical risks as they require recording electrodes to be implanted in or on the cortex and function well for long periods, which increases the risk of infection. Recording EEGs is a noninvasive method to monitor the brain's electrical activity. However, EEG signals feature a relatively low signal to noise ratio (SNR), a poor spatial resolution and they are contaminated by artifacts from various sources. These characteristics limit measuring the spatial distribution of brain electrical activity and thus necessitate significant preprocessing and post processing.

Recently, improvements have been made that render EEGs more accurate by increasing the spatial resolution [1]-[2]. One such improvement is the application of the surface Laplacian, the second spatial derivative, to the EEG. Tripolar concentric ring electrodes (TCREs), as shown in figure 4.1, automatically perform the Laplacian on the surface potentials. Previous studies have shown that EEGs obtained from TCRE's yield superior spatial selectivity, higher SNRs and better localization when compare to conventional EEG obtained with disc electrodes. These findings suggest that TCRE based EEGs may be beneficial for the analysis of neurological disorders [3]-[4]. However, due

to the proximity of the sensing elements, the TCRE requires significantly more resolution than a single element sensor.

The paper is organized as follows. Section II explains the digital tripolar concentric ring electrode (dTCRE) block diagram. The decimation ow pass filter that is built in FPGA is addressed in section III. Section IV presents the results and section V draws some conclusions.

4.2 Digital TCRE Electrode

Figure 4.1 illustrates the architecture of the digital tripolar concentric ring electrode (dTCRE). There are 3 parts to this novel electrode, a triplet of front-end sensors contacting the skin, a very low-noise pre-amplifier and a high-resolution analog-to-digital converter (ADC) with a single-bit output. The 1-bit format allows for easy multiplexing and subsequent wired or wireless transmission to a (remote) processing unit. The following two subsection describe the pre-amplifier and the data converter in more detail.

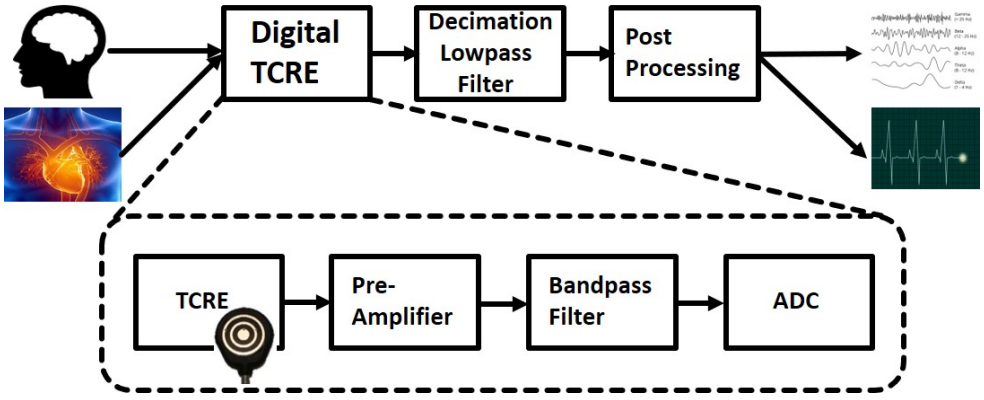

Figure 4.1. Active standalone tripolar concentric ring electrode (ACtE) block diagram

4.2.1 PreAmplifier

The self-noise of typical BJT or MOS amplifiers ramps up with decreasing frequency. This $\frac{1}{f}$ shaped noise characteristic is a particular problem when dealing with very low-frequency inputs such as biopotential signals.

Considering a frequency range from 1Hz to 2kHz, the best commercial pre-amplifiers feature a noise power density on the order of $10\frac{nV}{\sqrt{Hz}}$. This yields a total in-band noise voltage shy of 500 nV. We have decided to realize the pre-amplifier by means of the AD8295 chip. This device not only contains a low-noise instrumentation amplifier, but also 2 operational amplifiers (OA) and a pair of matched resistors. The additional components have been used to implement the anti-aliasing lowpass filter and to generate a fully-differential output for the subsequent ADC. The gain of the pre-amp, which is determined by an external resistor, has been set to 33. This yields an equivalent output noise voltage of approximately $15\mu V$ in the band of interest, i.e, 1Hz to 2kHz. To resolve signals that small, the ADC must provide a dynamic range of at least 100 dB.

4.2.2 Delta-Sigma Modulator

The data converter is realized by a Delta-sigma modulator (DSM), These noise-shaping data converters are well suited for applications where high resolution (above 14 bits) is critically important. A simple block diagram of a first-order DSM is shown in figure 4.2. In essence, the modulator subtracts a replica of its previous output signal from the current input, integrates this difference (hence delta-sigma) and finally subjects it to a very coarse quantization (frequently to a single bit) carried out at high-speed. In so doing, the low-frequency input signal is allowed to pass unhindered through the system while the dominant quantization noise is differentiated and thus strongly diminished in the very low-frequency range.

As hinted on in the previous paragraph, effectively shaping the quantization noise requires a high sampling rate in the final coarse quantizer. The high DSM output sampling rate f_s is typically described by the corresponding oversampling ratio (OSR), the quotient of applied sampling rate to Nyquist frequency $f_N = f_{max}$.

$$OSR = \frac{f_s}{f_N} \tag{4.1}$$

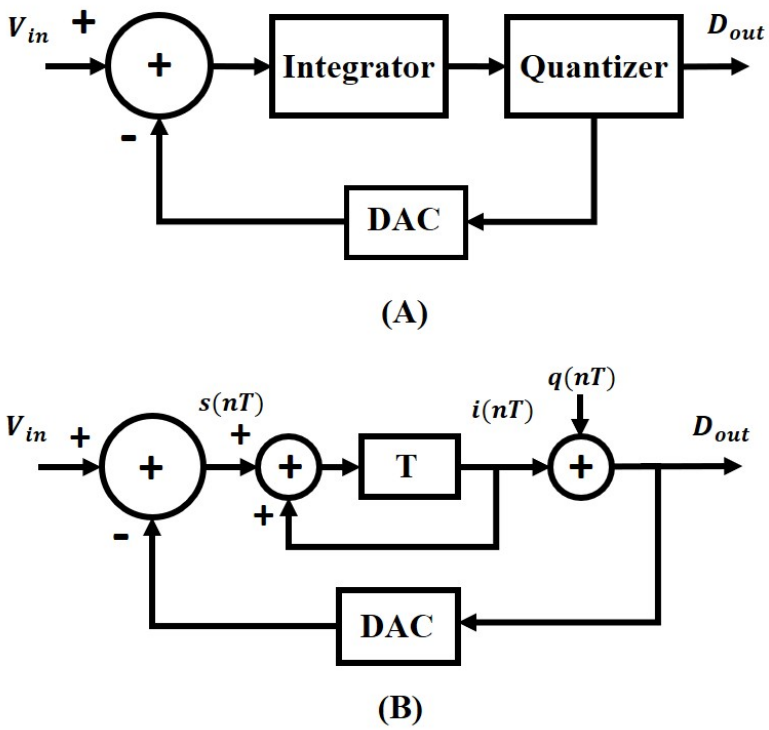

Figure 4.2. First-order ΔΣ modulator block diagram (A), discrete-time linearized first-order ΔΣ modulator block diagram (B)

Fig. 4.2A shows a block diagram of a first-oder DSM with an integrator and a quantizer in the forward path and a digital-to-analog converter (DAC) in the feedback path. Fig. 4.2B depicts a simplified block digram of a discrete-time first-order DSM, where the integrator is depicted as an accumulator and the quantizer is mimicked by an additive noise source. To reveal the noise shaping property of this configuration, one can describe the discrete-time output y(nT) as

$$y(nT) = x([n-1]T) + q(nT) - q([n-1]T) \tag{4.2}$$

where T denotes the sampling period. Transforming equation (2) into the z-domain yields

$$Y(z) = X(z)z^{-1} + Q(z)(1-z^{-1}) \tag{4.3}$$

This shows that the output of a discrete-time first-order modulator contains a delayed version of the input plus the difference of 2 consecutive quantization errors. By quantizing the modulator output at a very high rate (OSR times higher than necessary) the quantization error difference in the low-frequency range becomes very small. Conversely, quantization errors near $f_s/2$ are amplified. In other words, the modulator loop shapes the quantization noise by suppressing the low frequency components while enlarging the high-frequency components.

The dynamic range in the passband of a DSM can be further improved by employing a higher-order modulator loop filter, which discriminates more effectively between signal and quantization noise. An n^{th} order loop shapes the quantization noise as $(1-z^{-1})^n$ or $2^n sin(\pi fT)^n$. The suppression of the in-band quantization noise is therefore inversely proportional to OSR^{2n+1} [5]-[6].

The stated minimum dynamic range of 100 dB can be met by a third-order DSM with an OSR of 80. Figure 4.3 hows the block diagram of a third-order DSM using an inverse follow-the-leader (IFLF) topology. The DAC in the feedback path is realized by two switches connecting selecting $\pm V_{ref}$, respectively.

The corresponding switched-capacitor circuit is depicted in figure 4.4.

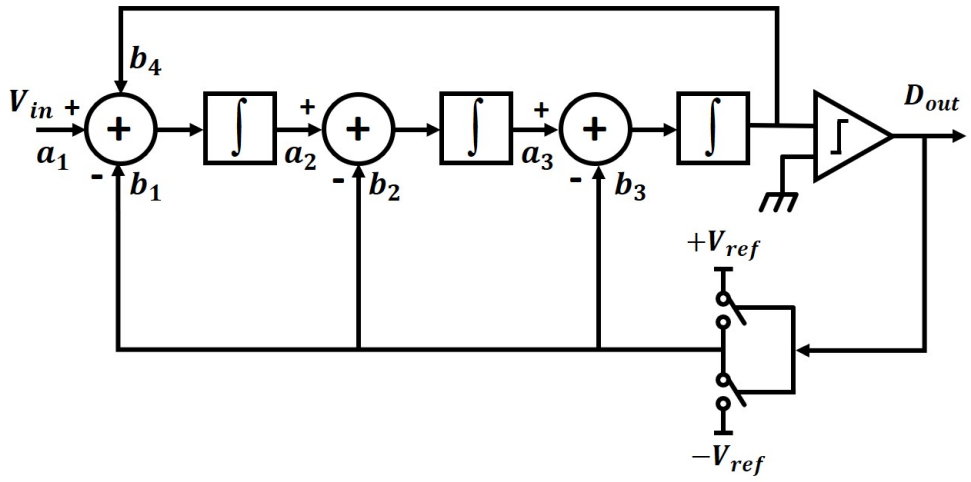

Figure 4.3. IFLF block diagram

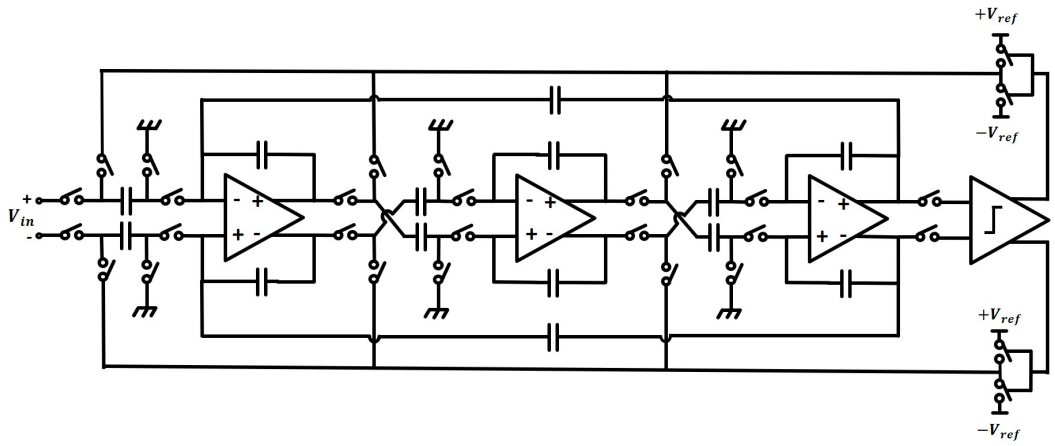

Figure 4.4. Switched capacitor implementation of the IFLF3

Assuming a maximum signal frequency of 1.5kHz requires a sampling rate of 240kHz. Figure 4.5 shows the output spectrum of the third-order modulator. As simulated with MATLAB, the frequency resolution in this plot is 1 Hz.

4.3 Digital Lowpass Filter and Decimator

To obtain a typical multi-bit digital output, the 1-bit stream of the DSM must be filtered digitally to remove the remaining out-of-band noise components and thus enable a reduction of the sampling rate.

In order to convert the 1-bit output of the DSM to a typical multi-bit digital signal, the modulator bit stream must first be lowpass filtered to render all out-of-band components irrelevant before the sampling rate can be reduced, otherwise, the out-of-band components would be aliased into the baseband.

A popular topology for the implementation of the lowpass filter/decimation stage is the running recursive sum (RRS) filter, also referred to as the cascaded integrator-comb (CIC) filter. An RRS or CIC filter is simply the recursive form of a finite impulse response (FIR) filter with equal coefficients:

$$H(z) = \frac{1}{D}\,\Sigma_{i=0}^{D}\, z^{-i} = \frac{1-z^{-D}}{1-z^{-1}} \tag{4.4}$$

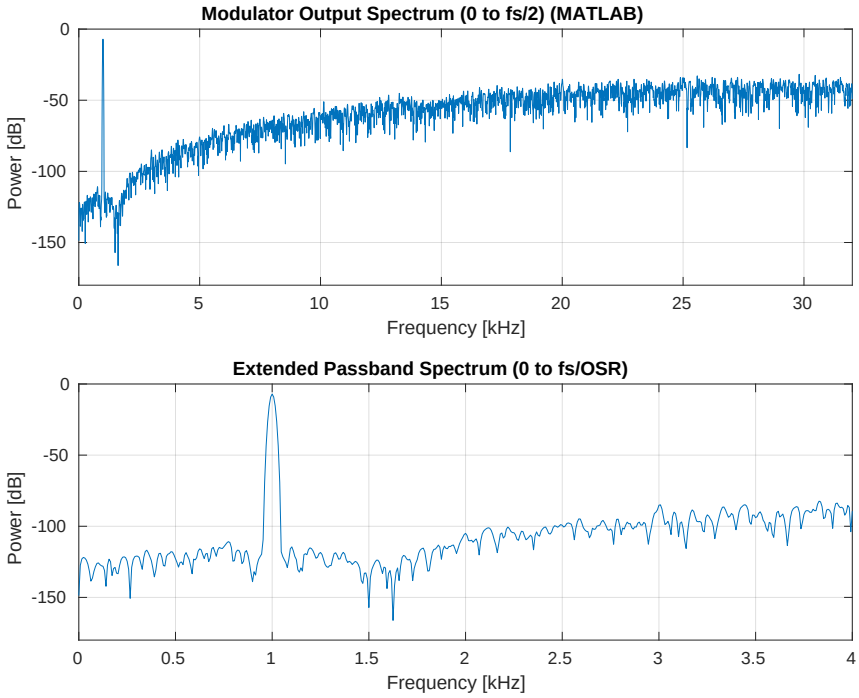

Figure 4.5. Modulator output spectrum using Matlab.

The hardware implementation of a CIC filter/decimation stage is simply the cascade of an accumulator clocked at $f_I = f_s$ and a differentiator operating with the reduced sampling rate $f_D = f_s/D$. Both blocks can readily be implemented using adders and registers, but no costly multipliers.

Since the order of the delta-sigma modulator is three, the CIC filter should at least be four to prevent excessive aliasing of out-of-band noise from the modulator entering the base-band. The schematic of the CIC digital filter that is implemented in the Altera SoC FPGA is illustrated in Fig. 4.6.

The CIC filters consists of N stages of cascaded integrators operating at the high sample rate (sampling frequency f_S), followed by N stages of cascaded differentiators operating at the lower sample rate, $\frac{f_s}{D}$, where D is the decimation factor. An integrator is a single-pole IIR filter with a unity feedback coefficient which in discrete-time domain can be shown as $y[n] = x[n] + y[n-1]$. Taking the z transform of both side yields

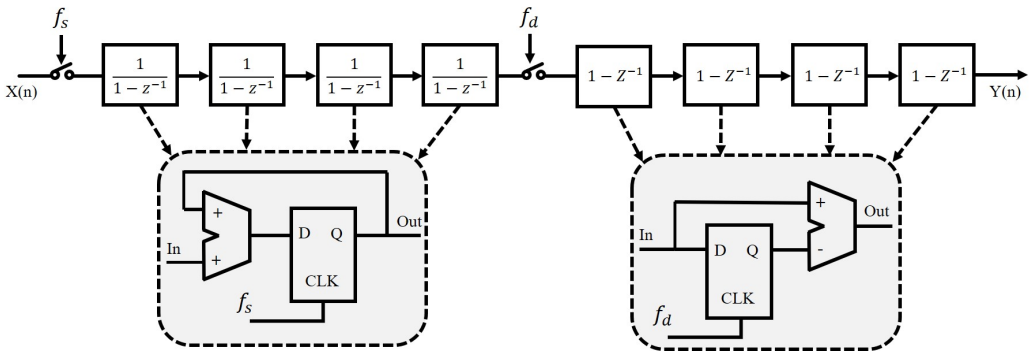

Figure 4.6. CIC filter block diagram

$$H_I = \frac{1}{1-Z^{-1}} \tag{4.5}$$

Moreover, the comb filter if an FIR filter that in discrete-time domain is described by $y[n] = x[n] - x[n-1]$. Taking the z transform of both side yields

$$H_C = 1 - Z^{-1} \tag{4.6}$$

The integrator and in comb filters can be simply implemented by an accumulator and a shift register as shown is Fig. 4.6. Thus the transfer function of the forth order CIC filter can be obtained

$$H(Z) = H_I^N(Z)H_C^N(Z) = \frac{1}{D^4}(\frac{1-Z^{-D}}{1-Z^{-1}})^4 \tag{4.7}$$

where D is the decimation factor.

As shown in Fig. 4.6, signal coming from the $\Delta\Sigma$ modulator $X(n)$ is a one bit stream with the frequency of $f_s = 200kHz$. This $X(n)$ passes through the four integrators operate at the sampling frequency $\frac{f_s}{D}$. The output from the fourth integrator is decimated down by a factor of D and fed to the input of the first differentiator and passes though the four differentiators operate at decimated clock frequency of $\frac{f_s}{D}$, where D is the decimation ratio. The relationship between the sampling frequency f_s. output data rate (DR) (or first notch frequency), and the decimation ratio D is given by:

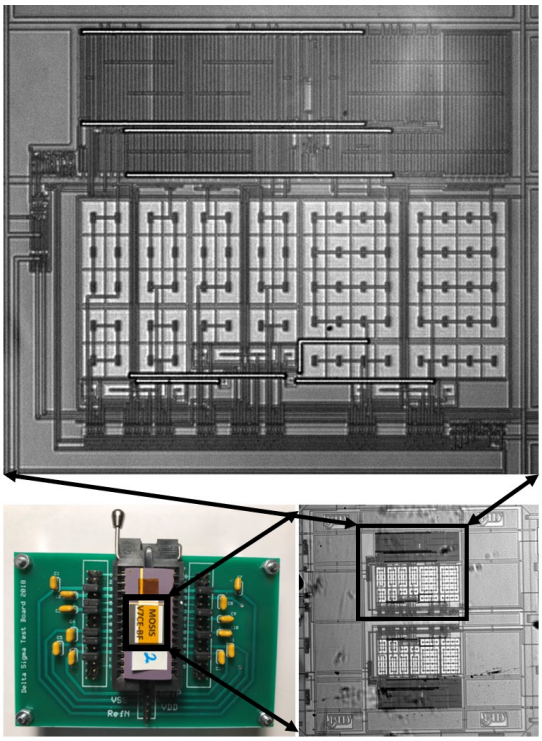

Figure 4.7. Delta-sigma modulator evaluation board and die photograph of the implemented IFLF3 modulator

$$DR = \frac{f_s}{D} \tag{4.8}$$

DR can be used to place a specific notch frequency in the digital CIC filter response. In our design, the first notch filter is at $4kHz$. Moreover,The output word size (bits) (B) from the CIC filter is given by:

$$B = N.log_2^D \tag{4.9}$$

Therefore, since a fouth order CIC filter is used and decimation factor is 64, our output word size is 24 bits. Besides, the gain of the CIC filter at dc is $Gain_{DC} = D^N$, which in our design the gain at dc is 50^4.

4.4 Results

The fully differetial switched capacitor delta sigma modulator has been designed using 0.5um CMOS technology. The fabrication was done by MOSIS. In order to measure the modulator, a pcb evaluation board has been designed as shown in Fig. 4.7. Each chip houses two modulator as required by each TCRE. The micrograph of the modulator is shown in Fig. 4.7. A digital analyzer has been utilized to record the modulator output. The recorded outputs were saved and plotted using MATLAB. A 1 kHz sinusoid has been applied to the input of the modulator and the clock frequency was 256 kHz. 20000 data points were saved and used to plot the FFT of out output. The results are shown in Fig. 4.8. Figure 4.9 shows one periode of the input. Signal clearly shows that for negative signals, the modulator output contains more zeros and for positive signals, the modulator output contains more ones. In between it contains an equal amount of ones and zeros.

The digital TCRE electrode is shown in Fig. 4.10. The system contains 2 boards

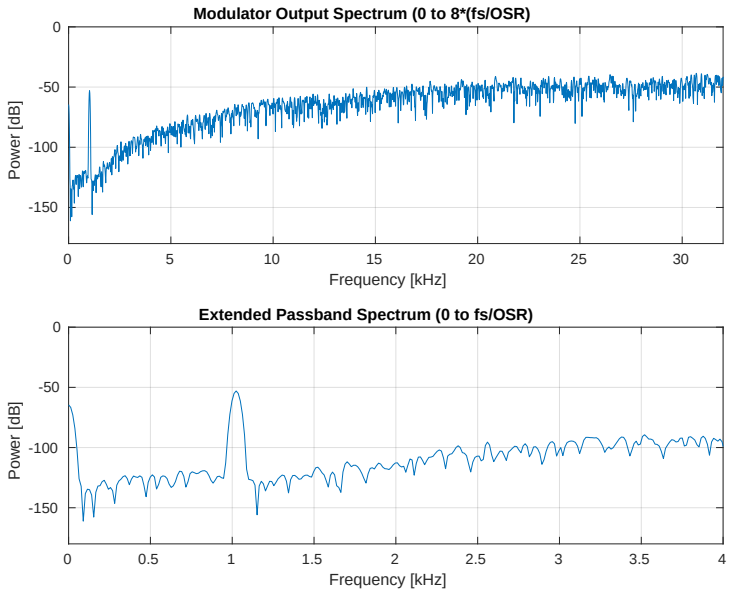

Figure 4.8. Spectrum measurement of the modulator

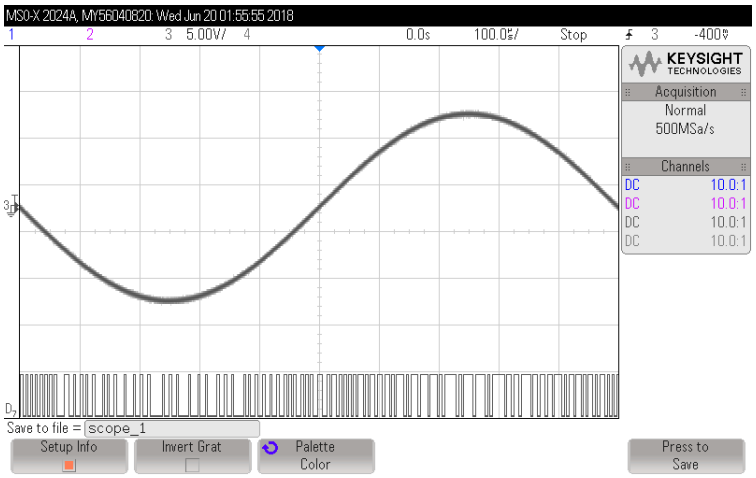

Figure 4.9. Implemented modulator output

that are stacked. Figure 4.10A and Fig. 4.10B illustrate the top and bottom layer of the bottom board respectively. The TCRE is located at the bottom layer to be in direct contact with the body and sense the biopotential signal. The pre-amplifiers are on the top side of this board. Figure 4.11C and Fig. 4.11D shown the bottom and top side of

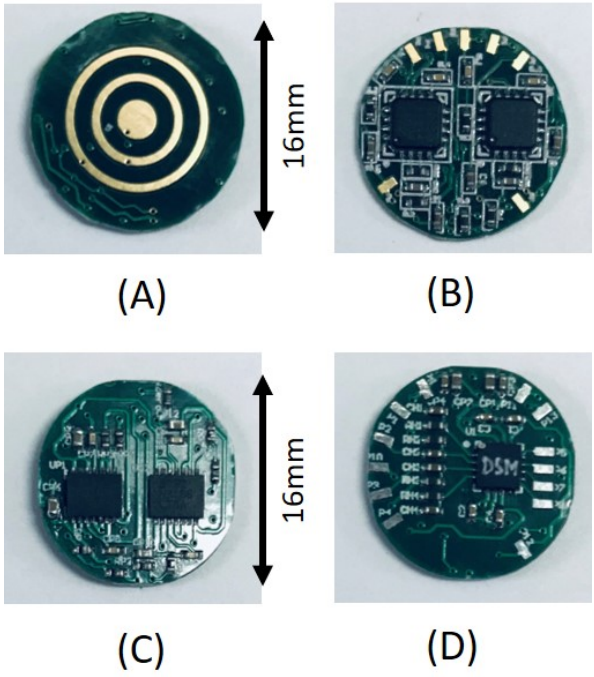

Figure 4.10. Delta-sigma modulator evaluation board and die photograph of the implemented IFLF3 modulator

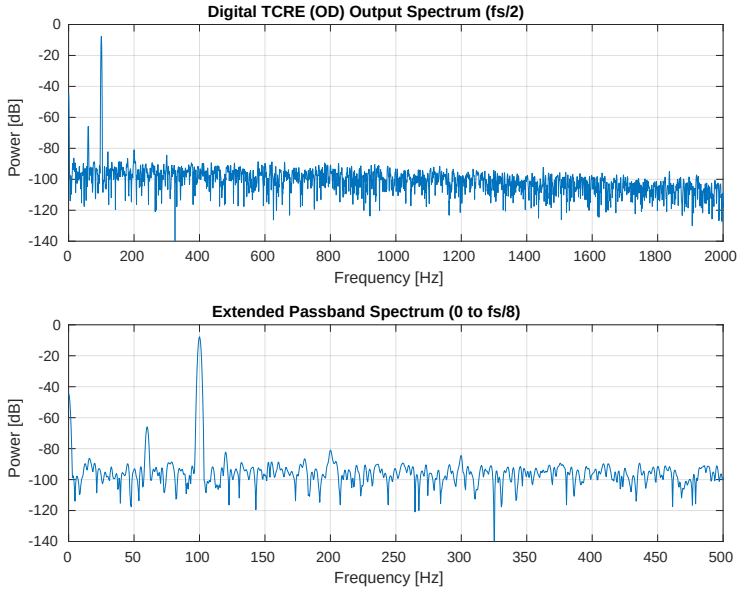

Figure 4.11. Spectrum measurement (OD) of the Digital TCRE and modulator with input of 30 mVpp

the top board. The regulators are located at the bottom side of this board. There are 2 regulators to provide $\pm 2.5V$ and $\pm 2V$, respectively. The modulator is placed on the top side of this board.

The 1-bit output of the modulator is connected to the FPGA for decimation/low pass filtering. To test the whole system, we have applied a signal of 30mVpp amplitude at a frequency of 100Hz directly to the preamplifier. The preamplifier has a gain of 33 and the output of the preamplifier is connected to the modulator. The output of the modulator is connected to the FPGA. The output data were saved and plotted using MATLAB. The results are shown in Fig. 4.11 and Fig. 4.12. Figure 4.11 shows the spectrum of the output while the input is applied between the outer ring and the disc electrode and Fig. 4.12 depicts the modulator output while the input is applied to the middle ring and the disc electrode. Figure 4.13 to Fig.4.16 reflects the same setup with lower input amplitudes. It should be mentioned that the decimated output sampling frequency is 4 kHz. All data vector for the FFT were 2^{13} points long.

4.5 Conclusion

In this study, a digital tripolar concentric ring electrode has been introduced. Each channel comprises a pre-amplified and a delta sigma modulator. The Cadence software tool suite was used to design, simulate, layout the delta sigma modulator. To minimize fabrication cost, our prototype chip has been fabricated through MOSIS (www.mosis.org), a service that provides access to fabrication of prototype and low-volume production quantities of integrated circuits at a comparatively low cost by combining designs from many customers onto a multi-project wafer. The one bit output is then connected to the FPGA to be decimated and low pass filtered. The altera DE1 SoC FPGA has been used to implement the decimation/low pass filter. As shown in Fig. 4.11-4.16, the spectral noise floor of the digital TCRE is approximately -100dB. This value is significantly higher than what MATLAB predicted in simulation. One of the reason of the excess noise is that MATLAB only depicts the noise related to the quantization noise. In order to make the simulation more realistic, other noise sources

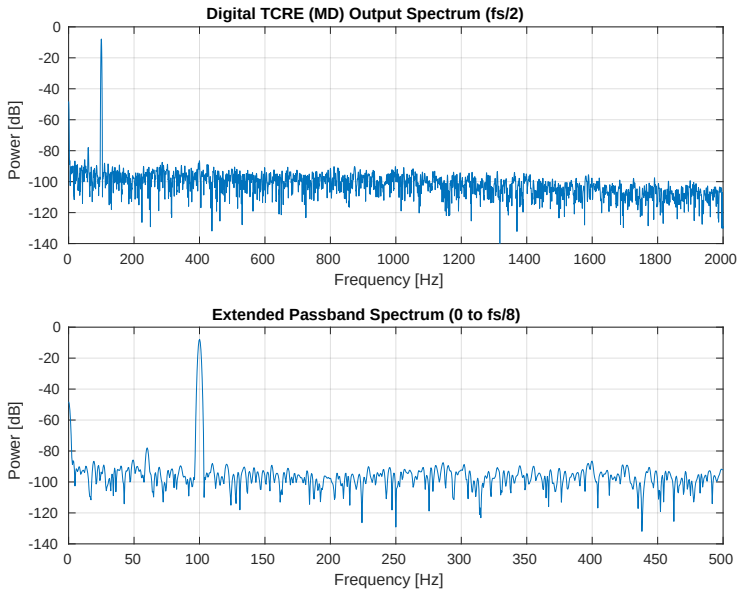

Figure 4.12. Spectrum measurement (MD) of the Digital TCRE and modulator with input of 30 mVpp

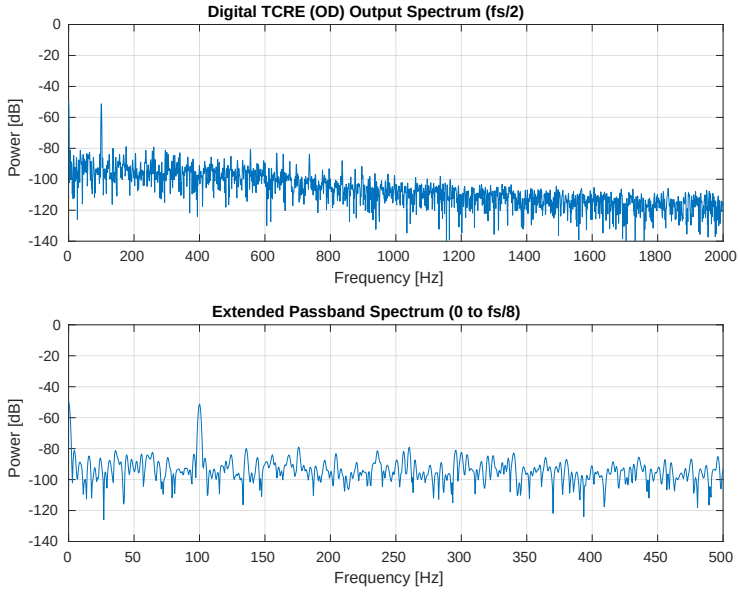

Figure 4.13. Spectrum measurement (OD) of the Digital TCRE and modulator with input of 200 uVpp

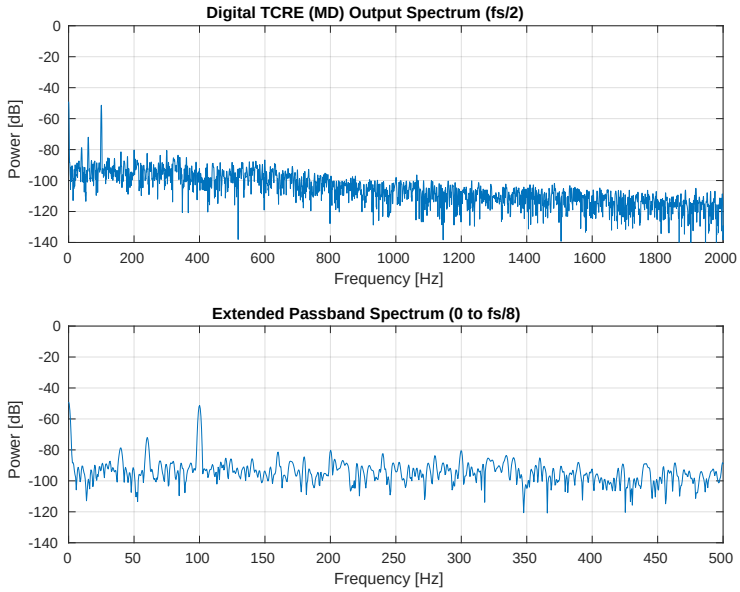

Figure 4.14. Spectrum measurement (MD) of the Digital TCRE and modulator with input of 200 uVpp

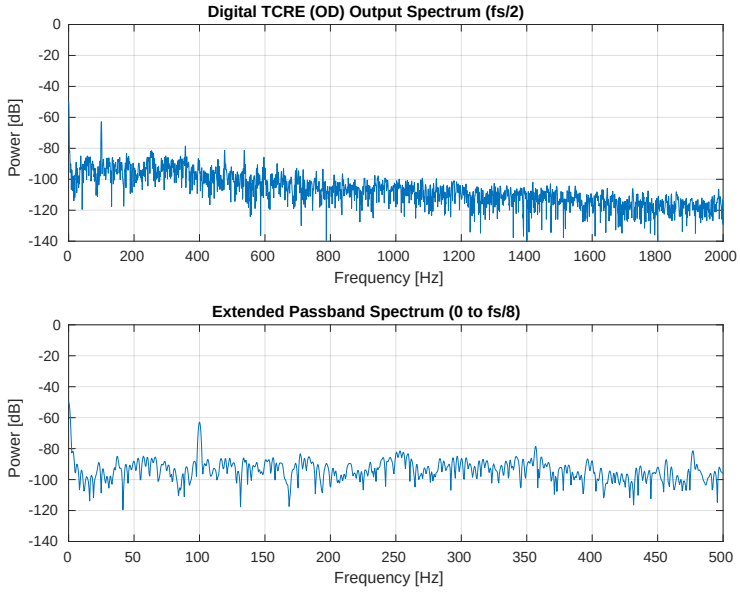

Figure 4.15. Spectrum measurement (OD) of the Digital TCRE and modulator with input of 50 uVpp

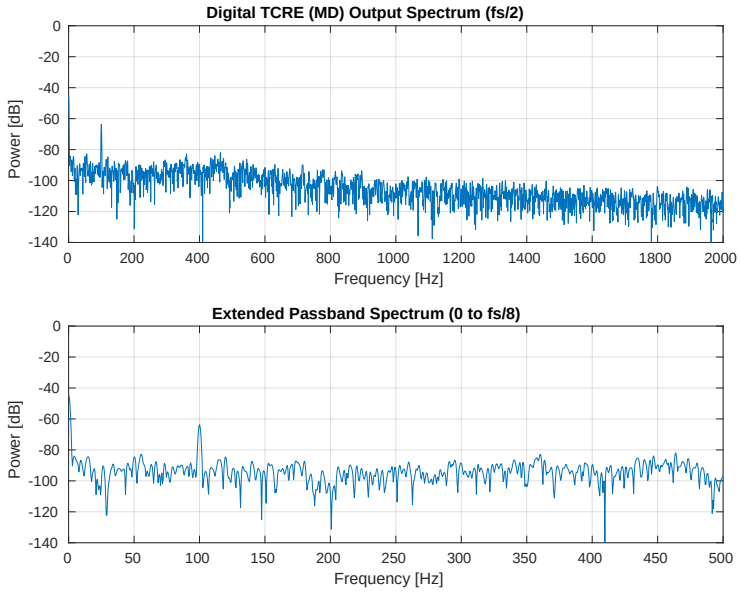

Figure 4.16. Spectrum measurement (MD) of the Digital TCRE and modulator with input of 50 uVpp

such as white noise should be taken into account. The other reason is that the boards are connected by wires before connected to the FPGA board. This can degrade the noise immunity of the system significantly.

[7, 8].

List of References

[1] J. E. Desmedt, V. Chalklin, and C. Tomberg, "Emulation of somatosensory evoked potential (sep) components with the 3-shell head model and the problem of ghost potential fields when using an average reference in brain mapping," *Electroencephalography and Clinical Neurophysiology/Evoked Potentials Section*, vol. 77, no. 4, pp. 243–258, 1990.

[2] P. Nunez, R. Silberstein, P. Cadusch, R. Wijesinghe, A. Westdorp, and R. Srinivasan, "A theoretical and experimental study of high resolution eeg based on surface laplacians and cortical imaging," *Electroencephalography and clinical neurophysiology*, vol. 90, no. 1, pp. 40–57, 1994.

[3] O. Makeyev, Q. Ding, S. M. Kay, and W. G. Besio, "Toward improving the laplacian estimation with novel multipolar concentric ring electrodes," in *Engineering in Medicine and Biology Society (EMBC), 2013 35th Annual International Conference of the IEEE*. IEEE, 2013, pp. 1486–1489.

[4] G. Besio, K. Koka, R. Aakula, and W. Dai, "Tri-polar concentric ring electrode development for laplacian electroencephalography," *IEEE transactions on biomedical engineering*, vol. 53, no. 5, pp. 926–933, 2006.

[5] A. J. Davis and G. Fischer, "Behavioral modeling of delta–sigma modulators," *Computer standards & interfaces*, vol. 19, no. 3-4, pp. 189–203, 1998.

[6] G. Fischer and A. J. Davis, "Delta-sigma modulators," *Encyclopedia of Electrical and Electronic Engineering*, vol. 19, pp. 244–254, 1999.

[7] K. L. Turabian, *A Manual for Writers of Term Papers, Theses, and Dissertations, 6th. edn.* Chicago, Illinois, United States of America: University of Chicago Press, 1987.

[8] University of Rhode Island. "A guide to producing your thesis with latex." June 2006. [Online]. Available: http://www.ele.uri.edu/info/thesis/guide

BIBLIOGRAPHY

Besio, G., Koka, K., Aakula, R., and Dai, W., "Tri-polar concentric ring electrode development for laplacian electroencephalography," *IEEE transactions on biomedical engineering*, vol. 53, no. 5, pp. 926–933, 2006.

Besio, G., Koka, K., Aakula, R., and Dai, W., "Tri-polar concentric ring electrode development for laplacian electroencephalography," *IEEE transactions on biomedical engineering*, vol. 53, no. 5, pp. 926–933, 2006.

Besio, G., Koka, K., Aakula, R., and Dai, W., "Tri-polar concentric ring electrode development for laplacian electroencephalography," *IEEE transactions on biomedical engineering*, vol. 53, no. 5, pp. 926–933, 2006.

Boccaletti, C., Castrica, F., Fabbri, G., and Santello, M., "A non-invasive biopotential electrode for the correct detection of bioelectrical currents," in *Proceedings of the Sixth IASTED International Conference on Biomedical Engineering*. ACTA Press, 2008, pp. 353–358.

Boccaletti, C., Castrica, F., Fabbri, G., and Santello, M., "A non-invasive biopotential electrode for the correct detection of bioelectrical currents," in *Proceedings of the Sixth IASTED International Conference on Biomedical Engineering*. ACTA Press, 2008, pp. 353–358.

Chang, J.-h., Park, J., Pak, Y. K., and Pak, J. J., "Fitting improvement using a new electrical circuit model for the electrode-electrolyte interface," in *Neural Engineering, 2007. CNE'07. 3rd International IEEE/EMBS Conference on*. IEEE, 2007, pp. 572–574.

Chang, J.-h., Park, J., Pak, Y. K., and Pak, J. J., "Fitting improvement using a new electrical circuit model for the electrode-electrolyte interface," in *Neural Engineering, 2007. CNE'07. 3rd International IEEE/EMBS Conference on*. IEEE, 2007, pp. 572–574.

Davis, A. J. and Fischer, G., "Behavioral modeling of delta–sigma modulators," *Computer standards & interfaces*, vol. 19, no. 3-4, pp. 189–203, 1998.

Desmedt, J. E., Chalklin, V., and Tomberg, C., "Emulation of somatosensory evoked potential (sep) components with the 3-shell head model and the problem of ghost potential fields when using an average reference in brain mapping," *Electroencephalography and Clinical Neurophysiology/Evoked Potentials Section*, vol. 77, no. 4, pp. 243–258, 1990.

Desmedt, J. E., Chalklin, V., and Tomberg, C., "Emulation of somatosensory evoked potential (sep) components with the 3-shell head model and the problem of ghost potential fields when using an average reference in brain mapping," *Electroencephalography and Clinical Neurophysiology/Evoked Potentials Section*, vol. 77, no. 4, pp. 243–258, 1990.

Desmedt, J. E., Chalklin, V., and Tomberg, C., "Emulation of somatosensory evoked potential (sep) components with the 3-shell head model and the problem of ghost potential fields when using an average reference in brain mapping," *Electroencephalography and Clinical Neurophysiology/Evoked Potentials Section*, vol. 77, no. 4, pp. 243–258, 1990.

Fernández-Corazza, M., Turovets, S., Luu, P., Price, N., Muravchik, C. H., and Tucker, D., "Skull modeling effects in conductivity estimates using parametric electrical impedance tomography," *IEEE Transactions on Biomedical Engineering*, vol. 65, no. 8, pp. 1785–1797, 2018.

Fischer, G. and Davis, A. J., "Delta-sigma modulators," *Encyclopedia of Electrical and Electronic Engineering*, vol. 19, pp. 244–254, 1999.

Franks, W., Schenker, I., Schmutz, P., and Hierlemann, A., "Impedance characterization and modeling of electrodes for biomedical applications," *IEEE Transactions on Biomedical Engineering*, vol. 52, no. 7, pp. 1295–1302, 2005.

Geddes, L., "Historical evolution of circuit models for the electrode-electrolyte interface," *Annals of biomedical engineering*, vol. 25, no. 1, p. 1, 1997.

Geddes, L., "Historical evolution of circuit models for the electrode-electrolyte interface," *Annals of biomedical engineering*, vol. 25, no. 1, p. 1, 1997.

Geddes, L. A., *Principles of applied biomedical instrumentation*. John Wiley & Sons, 1968.

Geddes, L. A. and Baker, L. E., *Principles of applied biomedical instrumentation*. John Wiley & Sons, 1989.

Gongadze, E., Petersen, S., Beck, U., and van Rienen, U., "Classical models of the interface between an electrode and an electrolyte," in *COMSOL Conference*, 2009, pp. 14–16.

Hirschorn, B., Orazem, M. E., Tribollet, B., Vivier, V., Frateur, I., and Musiani, M., "Constant-phase-element behavior caused by resistivity distributions in films i. theory," *Journal of The Electrochemical Society*, vol. 157, no. 12, pp. C452–C457, 2010.

Hirschorn, B., Orazem, M. E., Tribollet, B., Vivier, V., Frateur, I., and Musiani, M., "Constant-phase-element behavior caused by resistivity distributions in films i. theory," *Journal of The Electrochemical Society*, vol. 157, no. 12, pp. C452–C457, 2010.

Jochum, T., Denison, T., and Wolf, P., "Integrated circuit amplifiers for multi-electrode intracortical recording," *Journal of neural engineering*, vol. 6, no. 1, p. 012001, 2009.

Joye, N., Schmid, A., and Leblebici, Y., "Electrical modeling of the cell–electrode interface for recording neural activity from high-density microelectrode arrays," *Neurocomputing*, vol. 73, no. 1-3, pp. 250–259, 2009.

Kim, J. H., Song, I., Lee, S. M., Choi, H. S., Byeon, H., Kim, I., and Lee, S.-H., "An electroplating-free and minimal noise polyimide microelectrode for recording auditory evoked potentials from the epicranius," *IEEE Transactions on Biomedical Engineering*, vol. 60, no. 12, pp. 3425–3431, 2013.

Koka, K. and Besio, W. G., "Improvement of spatial selectivity and decrease of mutual information of tri-polar concentric ring electrodes," *Journal of neuroscience methods*, vol. 165, no. 2, pp. 216–222, 2007.

Koka, K. and Besio, W. G., "Improvement of spatial selectivity and decrease of mutual information of tri-polar concentric ring electrodes," *Journal of neuroscience methods*, vol. 165, no. 2, pp. 216–222, 2007.

Krizman, J., Skoe, E., and Kraus, N., "Stimulus rate and subcortical auditory processing of speech," *Audiology and Neurotology*, vol. 15, no. 5, pp. 332–342, 2010.

Makeyev, O., Ding, Q., Kay, S. M., and Besio, W. G., "Toward improving the laplacian estimation with novel multipolar concentric ring electrodes," in *Engineering in Medicine and Biology Society (EMBC), 2013 35th Annual International Conference of the IEEE*. IEEE, 2013, pp. 1486–1489.

Nasrollaholhosseini, S. H., Herrera, D. S., and Besio, W. G., "Impedance spectroscopy of tripolar concentric ring electrodes with ten20 and td246 pastes," in *Engineering in Medicine and Biology Society (EMBC), 2017 39th Annual International Conference of the IEEE*. IEEE, 2017, pp. 2426–2429.

Nasrollaholhosseini, S. H., Steele, P., and Besio, W. G., "Electrode-electrolyte interface model of tripolar concentric ring electrode and electrode paste," in *Engineering in Medicine and Biology Society (EMBC), 2016 IEEE 38th Annual International Conference of the*. IEEE, 2016, pp. 2071–2074.

Nasrollaholhosseini, S. H., Steele, P., and Besio, W. G., "Electrode-electrolyte interface model of tripolar concentric ring electrode and electrode paste," in *Engineering in Medicine and Biology Society (EMBC), 2016 IEEE 38th Annual International Conference of the*. IEEE, 2016, pp. 2071–2074.

Nunez, P., Silberstein, R., Cadusch, P., Wijesinghe, R., Westdorp, A., and Srinivasan, R., "A theoretical and experimental study of high resolution eeg based on surface laplacians and cortical imaging," *Electroencephalography and clinical neurophysiology*, vol. 90, no. 1, pp. 40–57, 1994.

Nunez, P., Silberstein, R., Cadusch, P., Wijesinghe, R., Westdorp, A., and Srinivasan, R., "A theoretical and experimental study of high resolution eeg based on surface laplacians and cortical imaging," *Electroencephalography and clinical neurophysiology*, vol. 90, no. 1, pp. 40–57, 1994.

Nunez, P., Silberstein, R., Cadusch, P., Wijesinghe, R., Westdorp, A., and Srinivasan, R., "A theoretical and experimental study of high resolution eeg based on surface laplacians and cortical imaging," *Electroencephalography and clinical neurophysiology*, vol. 90, no. 1, pp. 40–57, 1994.

Oostendorp, T. F., Delbeke, J., and Stegeman, D. F., "The conductivity of the human skull: results of in vivo and in vitro measurements," *IEEE transactions on biomedical engineering*, vol. 47, no. 11, pp. 1487–1492, 2000.

Toolan, T. M. and Tufts, D. W., "Detection and estimation in non-stationary environments," in *Proceedings IEEE Asilomar Conference on Signals, Systems & Computers*, Nov. 2003, pp. 797–801.

Turabian, K. L., *A Manual for Writers of Term Papers, Theses, and Dissertations, 6th. edn.* Chicago, Illinois, United States of America: University of Chicago Press, 1987.

University of Rhode Island. "A guide to producing your thesis with latex." June 2006. [Online]. Available: http://www.ele.uri.edu/info/thesis/guide

Wang, H. and Pilon, L., "Accurate simulations of electric double layer capacitance of ultramicroelectrodes," *The Journal of Physical Chemistry C*, vol. 115, no. 33, pp. 16 711–16 719, 2011.

Wang, H. and Pilon, L., "Accurate simulations of electric double layer capacitance of ultramicroelectrodes," *The Journal of Physical Chemistry C*, vol. 115, no. 33, pp. 16 711–16 719, 2011.

Zhang, R., McAllister, G., Scotney, B., McClean, S., and Houston, G., "Combining wavelet analysis and bayesian networks for the classification of auditory brainstem response," *IEEE Transactions on Information Technology in Biomedicine*, vol. 10, no. 3, pp. 458–467, 2006.